Physica D 56 (1992) 270–300
North-Holland

PHYSICA D

Homoclinic chaos in a laser–matter system

Darryl D. Holm and Gregor Kovačič[1]

Theoretical Division and Center for Nonlinear Studies, Los Alamos National Laboratory, MS B284, Los Alamos, NM 87545, USA

Received 9 July 1991
Revised manuscript received 9 January 1992
Accepted 9 January 1992
Communicated by H. Flaschka

In the slowly varying envelope approximation and the rotating wave approximation for the Maxwell–Schrödinger equations, we show that the presence of a small-amplitude probe laser in an excited, two-level, resonant medium leads to homoclinic chaos in the laser–matter dynamics.

1. Introduction

Haken [1] observed that the Maxwell–Bloch equations for the dynamics of a single cavity mode laser with two energy levels [2] could be transformed into the Lorenz equations, whose strange attractor and complex dynamics by now are famous in dynamical systems studies. Usually, lasers operate in the good cavity limit, in the regime of low dissipation. (For overviews of lasers and their dynamics, see refs. [3–6, 40].) In the low dissipation regime, laser output is very stable and corresponds to a limit-cycle solution of the Lorenz equations. The strange attractor behavior for the solutions of the laser equations appears only in the bad cavity limit [7] of high dissipation, but this limit is not of much practical value in laser operation.

Although the Haken transformation to the Lorenz equations seems not to be of much practical value, it does reveal the rich dynamical behavior that is latent in the laser equations. As we shall discuss, in the good cavity limit over time intervals much shorter than the characteristic relaxation times of the system, this rich dynamical behavior makes its appearance in the presence of perturbations, and when additional physics is introduced into the laser equations, such as additional cavity modes, more than two energy levels, or external forcing.

In the good cavity limit, several numerical studies [8–11], have addressed the issue of chaotic Hamiltonian dynamics in the interaction of atoms and molecules with self-consistently generated electromagnetic fields. These works have considered a generalization of the Jaynes–Cummings model [12, 13]; namely, an ensemble of two-level atoms interacting with a single-mode electromagnetic field. This model is known to be exactly solvable when retaining only the resonant interaction, that is, making the rotating wave approximation. These numerical studies find evidence for stochastic behavior of solutions of the generalized Jaynes–Cummings model. This stochastic behavior occurs in the numerical simulations above a threshold value of the coupling constant between the atoms and the field, and is apparently associ-

[1]Present address: Mathematical Sciences Department, Rensselaer Polytechnic Institute, Troy, NY 12180, USA.

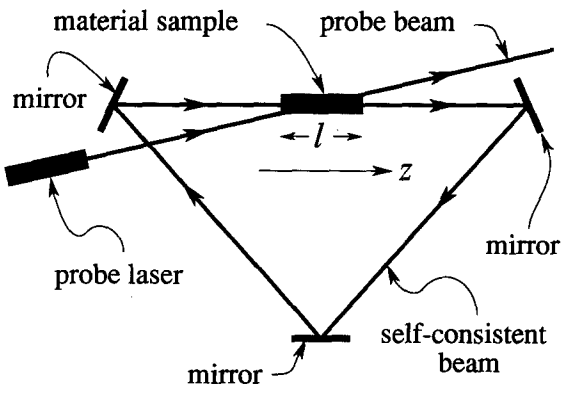

Fig. 1. Experimental arrangement for a probe laser interacting with a two-level material sample. The three mirrors form the single-mode ring-laser cavity. The probe beam is nearly collinear with the unidirectional self-consistent beam.

ated to the breakdown of the rotating wave approximation and the effects of nonresonant terms [8–10].

In contrast, the numerical study of Alekseev and Berman [11] investigates the Hamiltonian Maxwell–Bloch dynamics of a laser modeled as an ensemble of atoms in resonance with the self-consistent field of a single-mode cavity *within the rotating wave approximation*, and in interaction with a probe laser (an external monochromatic field of constant amplitude). The experimental arrangement for this investigation is sketched in fig. 1. The probe laser is assumed to have finite frequency detuning, but small amplitude. The numerical calculations of Alekseev and Berman [11] exhibit stochasticity caused by the probe laser perturbation, without any threshold condition in the coupling constant between the atoms and the field. These authors also give a heuristic and approximate analytical discussion of the stochasticity in terms of a pendulum model of the laser dynamics.

All these models impose some approximations upon a fundamental description that begins with Maxwell's equations for the electric field and Schrödinger's equation for the probability amplitudes of the atomic levels. The polarizability in Maxwell's equations is treated as an ensemble average of a quadratic function of the atomic amplitudes, neglecting quantum correlations. The rotating wave approximation is then imposed for the slowly varying complex envelopes of the solutions by averaging over their rapidly varying phases. The resulting Maxwell–Schrödinger envelope equations reduce to the Maxwell–Bloch equations in the rotating wave approximation, upon transforming to the phase-invariant variables known as Stokes parameters in classical optics (see ref. [14]). An early use of these phase invariant variables for deriving the Maxwell–Bloch equations appears in ref. [15]. Introduction of a probe-laser electric field as a perturbation in the Maxwell–Bloch dynamics results in the equations studied in ref. [11]. The model we study here is the Maxwell–Schrödinger envelope representation of this problem, which retains a certain phase information not present in the Maxwell–Bloch description.

The analysis presented in this paper is an exact analytical solution of the problem treated numerically in ref. [11]. The main result is an analytic demonstration of the mechanism causing chaos in this problem. Our analysis relies on the presence of symmetries leading to extra conservation laws in both the unperturbed Maxwell–Schrödinger envelope dynamics and the Maxwell–Schrödinger envelope dynamics perturbed by the probe laser. These symmetries and their associated conservation laws reduce the phase-space dimension by requiring the Maxwell–Schrödinger envelope dynamics to take place on intersections of the level surfaces of the conservation laws. These level surfaces provide a global geometrical framework for applying the Melnikov technique. The Melnikov technique establishes the presence of transverse intersections of stable and unstable manifolds of the hyperbolic periodic orbits in the perturbed Maxwell–Schrödinger envelope dynamics. Even under the perturbation, an extra conservation law remains. This extra conservation law constrains the solutions and determines the geometry of the transverse intersections, which arise in the presence of the perturbation. These transverse intersections imply chaotic motion of

phase points in their vicinity. The mechanism for the chaotic dynamics is established using a Smale horseshoe map. Specifically, we iterate initial condition sets lying on a cross-section transverse to the flow in the neighborhood of the intersection orbits. This iteration leads to chaotic dynamics on an invariant Cantor set by an extension of a construction due to Devaney [16]. In our construction of the Smale horseshoe map, the global phase-space geometry of the transverse intersections plays an explicit role. Namely, the transverse intersections can be thought of locally as a pair of spiral-saddle-focus connections (as discussed by Devaney [16]), crossed into a circle. However, to be realized globally, this local representation of the transverse intersections requires two charts. It is in these two charts that we construct the Smale horseshoe map for the perturbed Maxwell–Schrödinger envelope dynamics. The chaotic behavior we establish in this way may be seen experimentally as intermittent "flickering" of the light intensity emitted by the laser–matter system.

The rest of the paper is organized as follows. In section 2 the slowly varying envelope approximation and the rotating wave approximation for the self-consistently generated fields and the atomic level amplitudes are used to derive the Maxwell–Schrödinger envelope equations for laser dynamics as a six-dimensional set of canonical Hamiltonian equations on $\mathbb{C}^3$. The integrable phase space structure of this system is discussed in section 3, and explicit expressions are found for its homoclinic solutions. In particular, these homoclinic solutions are characterized globally in phase space as the stable and unstable manifolds of hyperbolic periodic orbits. In section 4 the hyperbolic periodic orbits are shown to persist under the small-amplitude probe-laser perturbation. In section 5 this perturbation is found by using the Melnikov vector method to cause the stable and unstable manifolds of these periodic orbits to intersect in $\mathbb{C}^3$. Transversality of these intersections is proven in section 6. Section 7 digresses to treat the case of a finite-amplitude probe laser with small detuning. Section 8 makes the Smale horseshoe construction for recurrent orbits. The Smale horseshoe is the mechanism for the chaotic dynamics present in this system. Conclusions and discussions of the measurability of this effect are given in section 9. The three appendices treat special cases and give background information that would otherwise interrupt the flow of the main text. Appendix A describes chaotic dynamics for a restricted, three-dimensional Maxwell–Bloch model. Appendix B discusses background on Poisson brackets and symplectic forms needed in the text. Finally, appendix C describes action principles for the Maxwell–Schrödinger equations and their perturbed envelope approximation.

2. Maxwell–Schrödinger envelope equations

In this section we derive the perturbed Maxwell–Schrödinger envelope model, whose investigation is the main topic of this paper. In particular, we derive this model by imposing the slowly varying envelope approximation and the rotating wave approximation directly on the primitive Maxwell–Schrödinger partial differential equations that describe the dynamics of the interaction between laser light and a material sample composed of two-level atoms. We present an alternative derivation of the perturbed Maxwell–Schrödinger envelope equations in appendix C. This second derivation is based on an action principle and accounts for the Hamiltonian nature of the perturbed Maxwell–Schrödinger envelope equations.

We consider the effects of a monochromatic probe laser interacting nearly resonantly with an excited ideal dielectric medium. The medium is modeled as a two-level atomic system dynamically changing under the influence of its own self-consistent electric field. Suppose the sample of excited dielectric material is of cylindrical shape, with length l and cross-sectional area A, and the resonant light in the medium has the wavelength

$\lambda = c/\omega_0$. One may assume that the electric field depends spatially only on the distance, z, along the optical axis (see fig. 1), provided the quantity $A/\lambda l$ is of order unity.

Assuming the electric field with magnitude E is linearly polarized, Maxwell's equations in the ideal dielectric material with $A/\lambda l = \mathcal{O}(1)$ reduce to the scalar wave equation

$$E_{zz} - \frac{1}{c^2}E_{tt} = \frac{4\pi}{c^2}P_{tt}.$$

In this equation, P denotes the polarizability of the material due to resonant or nearly resonant dipoles, and c is the speed of light in the host medium into which the (nearly) resonant dipoles are embedded. These dipoles are assumed to be so sparsely distributed in the host medium that they interact only with the imposed electric field and not with each other. This requires the dipole density n to satisfy the inequality $nd \ll E_0$, where E_0 is the typical magnitude of the electric field, and d is the atomic dipole moment.

We also assume that the distribution of resonant dipoles may be regarded as spatially continuous in z. This requires the dipole density to satisfy the inequality $nA\lambda \gg 1$. The requirements of the continuum approximation on one side, and the neglect of dipole–dipole interactions on the other, bracket the dipole density between the inequalities

$$\frac{E_0}{d} \gg n \gg \frac{1}{A\lambda}.$$

Schrödinger's equation

$$i\hbar\psi_t = \hat{H}\psi$$

governs the dynamics of an ensemble of two-level atoms interacting with the electric field E. In Schrödinger's equation the wave function ψ is expressible as

$$\psi = a_+(t,z)|+\rangle + a_-(t,z)|-\rangle,$$

where $|+\rangle$ represents the excited state, and $|-\rangle$ represents the ground state of the atoms. In the expression for the wave function ψ, the quantities $a_+(t,z)$ and $a_-(t,z)$ are the probability amplitudes for $nA\,\Delta z$ dipoles in a slice of the sample of width Δz at position z to be in the states $|+\rangle$ and $|-\rangle$, respectively.

The Hamiltonian describing the two-level system with dipole-field interactions takes the matrix form

$$\hat{H} = \begin{pmatrix} \frac{1}{2}\hbar\omega_0 & -dE \\ -dE & -\frac{1}{2}\hbar\omega_0 \end{pmatrix}.$$

With this Hamiltonian, Schrödinger's equation implies the following equations for the complex amplitudes $a_+(t,z)$ and $a_-(t,z)$:

$$i\dot{a}_+ = \frac{\omega_0}{2}a_+ - \frac{dE}{\hbar}a_-, \quad i\dot{a}_- = -\frac{\omega_0}{2}a_- - \frac{dE}{\hbar}a_+,$$

with time derivatives denoted as overdots.

We now introduce the *cooperative frequency*

$$\omega_c = \sqrt{\frac{2\pi n d^2 \omega_0}{\hbar}}$$

as the basic frequency scale, and nondimensionalize by the following replacements:

$$t \to \omega_c t, \quad z \to \frac{\omega_c z}{c}, \quad E \to \frac{dE}{\hbar\omega_c}.$$

By definition, the macroscopic polarizability P is the expected value of the microscopic dipole moment times the dipole density. Hence,

$$P = nd(a_+a_-^* + a_+^*a_-).$$

We thus obtain the *dimensionless Maxwell–Schrödinger equations*

$$E_{zz} - E_{tt} = 2\kappa(a_+a_-^* + a_+^*a_-)_{tt},$$

$$i\dot{a}_+ = \frac{1}{2\kappa}a_+ - Ea_-, \quad i\dot{a}_- = -\frac{1}{2\kappa}a_- - Ea_+,$$

where $\kappa = \omega_c/\omega_0$. From here on, we will assume that the ratio κ is small, $\kappa \ll 1$[#1].

In order to set up the rotating wave approximation, we assume a solution in the form of a modulated right-going wave,

$$E = \mathscr{E}\, e^{-i(t-z)/\kappa} + \mathscr{E}^* e^{i(t-z)/\kappa} + \epsilon\, e^{-i(t-z)/\kappa'} + \epsilon\, e^{i(t-z)/\kappa'},$$
$$a_+ = b_+ e^{-i(t-z)/2\kappa}, \quad a_- = b_- e^{i(t-z)/2\kappa}.$$

The first two terms in the modulated traveling-wave expression for E represent the self-consistently generated electric field, and the second two terms denote the probe-laser field. The rapidly varying phase factors in each term of E represent the color of the laser light, while the amplitude factors represent its slowly varying brightness. The dimensionless frequency detuning between the self-consistent field of the resonant medium and the probe laser is given by $1/\kappa - 1/\kappa' = \omega = \mathscr{O}(1)$. Following Alekseev and Berman [11], we assume that the complex envelope functions $\mathscr{E}$, b_+ and b_- depend only on time. The equations for the slowly varying probability amplitudes $b_+(t)$ and $b_-(t)$ become

$$i\dot{b}_+ = -(\mathscr{E} + \epsilon\, e^{i\omega(t-z)})b_- - (\mathscr{E}^* + \epsilon\, e^{-i\omega(t-z)})b_-\, e^{2i(t-z)/\kappa},$$
$$i\dot{b}_- = -(\mathscr{E}^* + \epsilon\, e^{-i\omega(t-z)})b_+ - (\mathscr{E} + \epsilon\, e^{i\omega(t-z)})b_+\, e^{-2i(t-z)/\kappa}.$$

The rotating wave approximation is imposed by averaging these equations over the fast phase $(t-z)/\kappa$. After averaging the amplitude equations, we find

$$i\dot{b}_+ = -(\mathscr{E} + \epsilon\, e^{i\omega(t-z)})b_-,$$
$$i\dot{b}_- = -(\mathscr{E}^* + \epsilon\, e^{-i\omega(t-z)})b_+.$$

In the scalar wave equation for the electric field E, we assume that $\mathscr{E}$, b_+ and b_- vary slowly in time and that therefore the inequalities $\dot{\mathscr{E}} \ll \mathscr{E}/\kappa$, etc., hold. This assumption drops the order of the wave equation to first order. The equation we thus obtain is

$$i\dot{\mathscr{E}}\, e^{-i(t-z)/\kappa} - i\dot{\mathscr{E}}\, e^{i(t-z)/\kappa} = -\left(b_+ b_-^*\, e^{-i(t-z)/\kappa} + b_+^* b_-\, e^{i(t-z)/\kappa}\right).$$

Collecting terms with the same phase factor as $\dot{\mathscr{E}}$, yields

$$i\dot{\mathscr{E}} = -b_+ b_-^*.$$

The assumption that $\mathscr{E}$ and $b_\pm$ are independent of z becomes consistent after averaging the equations just obtained in z. This spatial averaging introduces only negligible errors, provided the sample is sufficiently short; in particular, provided the sample lies between the (nondimensional values) $-z_0$ and z_0, where

$$z_0 = \frac{\omega_c l}{2c} \ll 1.$$

We thus obtain the *perturbed Maxwell–Schrödinger envelope equations*

$$\dot{\mathscr{E}} = i b_+ b_-^*, \tag{2.1a}$$
$$\dot{b}_+ = i(\mathscr{E} + \epsilon\, e^{i\omega t})b_-, \tag{2.1b}$$
$$\dot{b}_- = i(\mathscr{E}^* + \epsilon\, e^{-i\omega t})b_+. \tag{2.1c}$$

The analysis of these perturbed Maxwell–Schrödinger envelope equations is the subject of the remainder of the paper[#2].

The perturbed Maxwell–Schrödinger envelope equations (2.1) form a Hamiltonian system with

[#1] This is a typical assumption in the dynamics of short laser pulses in fibers. In fact, taking $d = 1$ Debye ($= 10^{-18}$ esu), and $\omega_0 = 10^{15}$ Hz for visible light gives $\omega_c(\mathrm{Hz}) = 2 \times 10^3 \sqrt{n(\mathrm{cm}^{-3})}$. So $\kappa \ll 1$, so long as the dipole number density n satisfies $\sqrt{n(\mathrm{cm}^{-3})} \ll 10^{12}$.

[#2] Note: Transforming these equations to *Stokes parameters* R_x, R_y, and R_z, given by $R_z = |b_+|^2 - |b_-|^2$, $R_x + iR_y = 2ib_+b_-^*$, recovers the perturbed Maxwell–Bloch model studied numerically by Alekseev and Berman [11]. See also appendix A and appendix B.

time-dependent Hamiltonian function given by the electromagnetic interaction energy,

$$\mathscr{H} = -\tfrac{1}{2}(\mathscr{E} + \epsilon e^{i\omega t})b_+^* b_- - \tfrac{1}{2}(\mathscr{E}^* + \epsilon e^{-i\omega t})b_+ b_-^*,$$

and complex symplectic form $-(1/2i)(d\mathscr{E} \wedge d\mathscr{E}^* + db_+ \wedge db_+^* + db_- \wedge db_-^*)$. (See appendix B for a discussion of symplectic forms, Poisson brackets, and their connection to Hamiltonian systems.)

Invariance of the Hamiltonian $\mathscr{H}$ under the transformation

$$(\mathscr{E}, b_+, b_-) \mapsto (\mathscr{E}, b_+ e^{i\gamma}, b_- e^{i\gamma}),$$

for any angle γ, implies the conservation of the sum $L = \frac{1}{2}|b_+|^2 + \frac{1}{2}|b_-|^2$. This conservation reflects preservation in the rotating wave approximation of unitarity of the averaged probability amplitudes in (2.1).

The perturbed Maxwell–Schrödinger envelope equations (2.1) simplify upon using the time-dependent canonical transformation

$$\mathscr{E} = (x - \epsilon)e^{i\omega t}, \quad b_+ = u e^{2i\omega t}, \quad b_- = v e^{i\omega t}.$$

This canonical transformation brings eqs. (2.1) into the autonomous form

$$\dot{x} = -i\omega(x - \epsilon) + iuv^*, \tag{2.2a}$$

$$\dot{u} = -2i\omega u + ixv, \tag{2.2b}$$

$$\dot{v} = -i\omega v + ix^* u. \tag{2.2c}$$

The system (2.2) is Hamiltonian with the *time-independent* Hamiltonian function

$$H = \tfrac{1}{2}\omega|x - \epsilon|^2 + \omega|u|^2 + \tfrac{1}{2}\omega|v|^2 - \tfrac{1}{2}xu^*v - \tfrac{1}{2}x^*uv^*, \tag{2.3}$$

and complex symplectic form $-(1/2i)(dx \wedge dx^* + du \wedge du^* + dv \wedge dv^*)$. It follows that the function H is a constant of motion for both (2.2) and also the equivalent equations (2.1) in the $(\mathscr{E}, b_+, b_-)$ coordinates. In these original coordinates, H can be written as $H = \Xi + \frac{3}{4}\omega L$ with

$$\Xi = \tfrac{1}{2}\omega|\mathscr{E}|^2 + \tfrac{1}{4}\omega(|b_+|^2 - |b_-|^2) - \tfrac{1}{2}\left[(\mathscr{E} + \epsilon e^{i\omega t})b_+^* b_- + (\mathscr{E}^* + \epsilon e^{-i\omega t})b_+ b_-^*\right].$$

The first term in this expression represents the energy of the self-consistent electric field; the second term is the excitation energy of the atoms; and the third term is $\mathscr{H}$, the electromagnetic interaction energy between the total electric field and the ensemble of atomic dipole moments. Thus the conserved quantity Ξ is the total energy for the perturbed Maxwell–Schrödinger envelope equations.

There are two integrable limits of the Hamiltonian system (2.1), namely, $\epsilon = 0$ and $\omega = 0$. The first limit corresponds to zero amplitude of the laser probe, and the second to zero detuning but finite probe amplitude. In what follows, we investigate the two near-integrable cases, $\epsilon \ll 1$ and $\omega \ll 1$, always assuming that $\kappa \ll \epsilon$ and $\kappa \ll \omega$. We first treat the case of small ϵ in detail. Later, in section 7, we briefly discuss the case of small ω, whose analysis follows along the same lines.

3. Unperturbed homoclinic structure

In this section we determine the homoclinic orbit structure of the unperturbed system (2.2) with $\epsilon = 0$, namely,

$$\dot{x} = -i\omega x + iuv^*, \tag{3.1a}$$

$$\dot{u} = -2i\omega u + ixv, \tag{3.1b}$$

$$\dot{v} = -i\omega v + ix^* u. \tag{3.1c}$$

This unperturbed Maxwell–Schrödinger envelope system possesses three constants of motion

$$H = \tfrac{1}{2}\omega|x|^2 + \omega|u|^2 + \tfrac{1}{2}\omega|v|^2 - \tfrac{1}{2}xu^*v - \tfrac{1}{2}x^*uv^*,$$
$$L = \tfrac{1}{2}|u|^2 + \tfrac{1}{2}|v|^2, \quad J = \tfrac{1}{2}|x|^2 + \tfrac{1}{2}|u|^2.$$

The first three terms of the Hamiltonian H generate the phase rotation

$$(x,u,v) \mapsto (x\,e^{i\omega t}, u\,e^{2i\omega t}, v\,e^{i\omega t})$$

discussed earlier. Of course, in the limit when the detuning, ω, vanishes, these terms are absent.

We next use the two constants of motion L and J to reduce the order of the unperturbed system (3.1). In particular, we reduce the unperturbed problem to phase-plane analysis, in which all the homoclinic orbits are readily identified and solutions on these orbits are calculated. The full homoclinic solutions in our original phase space are then reconstructed by quadratures from those in the reduced phase plane. We discuss their geometry in detail, because of its importance as a framework for the treatment of the perturbed problem.

The reduction of order in the unperturbed problem (3.1) is achieved by introducing the following canonical transformation, which is defined for $|\chi| < \min(2L, 2J)$:

$$x = \sqrt{2J - |\chi|^2}\, e^{i\psi}, \tag{3.2a}$$

$$u = \chi\, e^{i(\psi+\theta)}, \tag{3.2b}$$

$$v = \sqrt{2L - |\chi|^2}\, e^{i\theta}. \tag{3.2c}$$

The Hamiltonian H in these new variables becomes

$$H = \omega L + \omega J - \tfrac{1}{2}\sqrt{2L - |\chi|^2}\,\sqrt{2J - |\chi|^2}\,(\chi + \chi^*), \tag{3.3}$$

and the new symplectic form is $-(1/2i)\,d\chi \wedge d\chi^* + dJ \wedge d\psi + dL \wedge d\theta$. Note that the transformation (3.2) is singular on $|\chi|^2 = \min(2L, 2J)$. This singularity is similar to the singularity at the origin of the usual planar polar coordinates.

Since L and J are constants of motion, their conjugate angles ψ and θ, respectively, do not enter the Hamiltonian H. Therefore, these angles are also not present in any right-hand sides of the equations of motion. In particular, ψ and θ do not appear in the equation for χ. Hence, we can calculate ψ and θ by quadratures, once we have solved the planar system for the complex scalar χ.

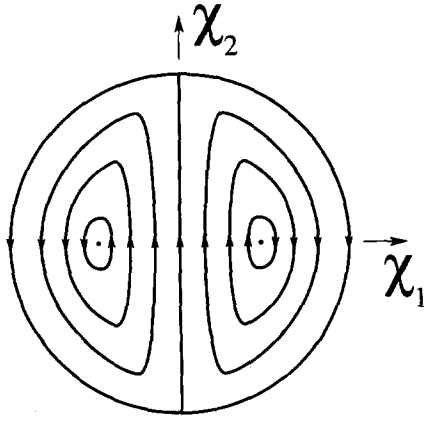

Fig. 2. Phase portrait for the unperturbed Maxwell–Schrödinger envelope system in the reduced phase plane, (χ_1, χ_2). The vertical line segment along the χ_2-axis is a homoclinic orbit when the two constants of motion J and L are equal.

We obtain the phase portrait of the equations for χ by calculating the level lines of the Hamiltonian (3.3) at fixed values of J and L. This phase portrait is presented in fig. 2, where χ_1 and χ_2 represent the real and imaginary components of χ, respectively. The canonical Poisson bracket relation between χ_1 and χ_2 is $\{\chi_2, \chi_1\} = 1$, corresponding to the real symplectic form $d\chi_1 \wedge d\chi_2$.

Fig. 2 suggests that the line segment $\{(\chi_1, \chi_2) | \chi_1 = 0,\ \chi_2^2 < \min(2L, 2J)\}$ is a likely candidate for a homoclinic orbit. The equation for χ_2 on that line segment is

$$\dot{\chi}_2 = \sqrt{(2J - \chi_2^2)(2L - \chi_2^2)}\,.$$

In most cases the solutions of this equation are elliptic functions, which are periodic in t. In such cases, the line segment $\{(\chi_1, \chi_2) | \chi_1 = 0,\ \chi_2^2 < \min(2L, 2J)\}$ represents a segment of a periodic orbit. The only case when homoclinic orbits ap-

pear is when $L = J$. Then we have

$$\dot{\chi}_2 = 2L - \chi_2^2,$$

with a particular solution

$$\chi_2 = \sqrt{2L}\,\tanh(\sqrt{2L}\,t). \tag{3.4}$$

The other solutions on the homoclinic orbits can be obtained from (3.4) by shifting time t to $t - t_0$, where t_0 is an arbitrary constant. On the line segment $\{(\chi_1, \chi_2)|\chi_1 = 0,\ \chi_2^2 < \min(2L, 2J)\}$, the equations for ψ and θ become $\dot{\psi} = \dot{\theta} = -\omega$. Therefore, the solutions for the angles ψ and θ associated to the solution (3.4) are $\psi = -\omega t + \psi_0$ and $\theta = -\omega t + \theta_0$.

Returning to the (x, u, v) coordinates via eqs. (3.2) and using the quadrature relations for ψ and θ, allows the homoclinic solutions (3.4) to be expressed in the original phase space as

$$x = \sqrt{2L}\,\mathrm{sech}(\sqrt{2L}\,t)\,e^{i(-\omega t + \psi_0)}, \tag{3.5a}$$

$$u = i\sqrt{2L}\,\tanh(\sqrt{2L}\,t)\,e^{i(-2\omega t + \psi_0 + \theta_0)}, \tag{3.5b}$$

$$v = \sqrt{2L}\,\mathrm{sech}(\sqrt{2L}\,t)\,e^{i(-\omega t + \theta_0)}. \tag{3.5c}$$

Because the system (3.1) is autonomous, all the other solutions on the same orbit are again obtained by shifting time t to $t - t_0$.

Formulae (3.5) describe a three-parameter family of homoclinic orbits parametrized by L, ψ_0 and θ_0. These orbits are homoclinic to the periodic orbits O^L, given by

$$x = 0, \quad u = i\sqrt{2L}\,e^{i(-2\omega t + \text{constant})}, \quad v = 0.$$

In particular, the solution (3.5) approaches the trajectory with $u = -i\sqrt{2L}\,e^{i(-2\omega t + \psi_0 + \theta_0)}$ for $t \to -\infty$, and the trajectory with $u = i\sqrt{2L}\,e^{i(-2\omega t + \psi_0 + \theta_0)}$ for $t \to \infty$. Both of these limiting trajectories lie on the same orbit O^L, which is a circle of radius $\sqrt{2L}$ in the complex u-plane. When $\omega = 0$, the orbit O^L is a circle of fixed points, and the solutions (3.5) with $\omega = 0$ are heteroclinic orbits connecting antipodal points on that circle. (See fig. 3.)

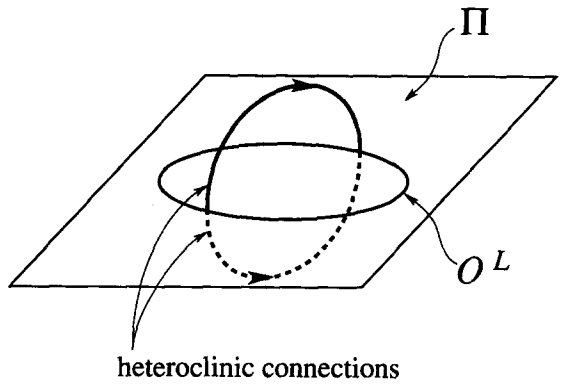

Fig. 3. For zero detuning, ω, opposite pairs of points on the circle of equilibria O_ϵ^L in the u-plane Π are connected by heteroclinic orbits.

Having found the homoclinic solutions (3.5), we now turn to a geometric description of their global phase space structure. We first observe that the periodic orbits O^L (given above) foliate the complex u-plane, denoted $\Pi = \{(x, u, v)|x = v = 0\}$. Each orbit O^L possesses a three-dimensional stable and three-dimensional unstable manifold, $\mathscr{W}^s(O^L)$ and $\mathscr{W}^u(O^L)$, respectively. These two manifolds coincide to form a three-dimensional homoclinic manifold $\mathscr{W}(O^L)$. The manifold $\mathscr{W}(O^L)$ can either be parametrized by the parameters t, ψ_0 and θ_0 in eqs. (3.5) with a fixed value of L, or can be described implicitly by the equations

$$\omega L + \omega J - H = 0, \tag{3.6a}$$

$$J - L = 0, \tag{3.6b}$$

$$L = \text{constant}, \tag{3.6c}$$

which hold on the orbit O^L and, therefore, by continuity also on the manifold $\mathscr{W}(O^L)$. In the (x, u, v) coordinates, eqs. (3.6) describing the homoclinic manifold $\mathscr{W}(O^L)$ become

$$\tfrac{1}{2}xu^*v + \tfrac{1}{2}x^*uv^* = 0, \tag{3.7a}$$

$$\tfrac{1}{2}|x|^2 - \tfrac{1}{2}|v|^2 = 0, \tag{3.7b}$$

$$\tfrac{1}{2}|u|^2 + \tfrac{1}{2}|v|^2 = \text{constant}. \tag{3.7c}$$

Heuristically, each homoclinic manifold $\mathscr{W}(O^L)$

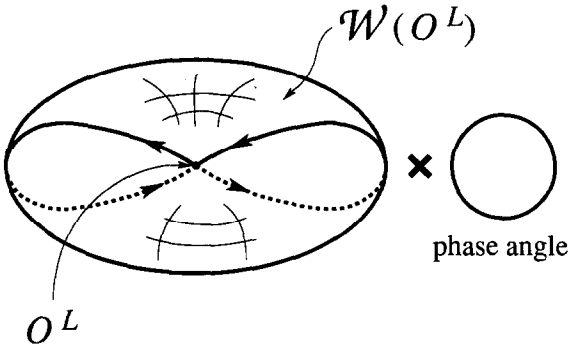

Fig. 4. Each homoclinic manifold $\mathcal{W}(O^L)$ is the Cartesian product of a "pinched" two-torus and a circle. The unstable periodic orbit O^L lies at the center of the pinched torus.

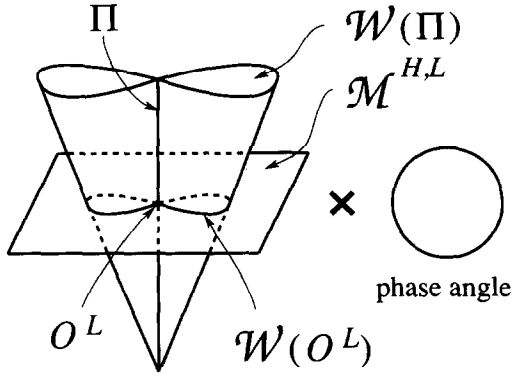

Fig. 5. The union of the homoclinic manifolds $\mathcal{W}(O^L)$ is the four dimensional homoclinic manifold $\mathcal{W}(\Pi)$, connecting the u-plane Π to itself. A given homoclinic manifold $\mathcal{W}(O^L)$ lies on a manifold $\mathcal{M}^{H,L}$, which is an intersection of level surfaces of the conserved quantities H and L.

can be thought of as the Cartesian product of a "pinched" two-torus and a circle. (See fig. 4.)

The union of the manifolds $\mathcal{W}(O^L)$ is the four-dimensional homoclinic manifold $\mathcal{W}(\Pi)$, connecting the u-plane Π to itself. The manifold $\mathcal{W}(\Pi)$ can now be parametrized by eqs. (3.5) using all four parameters, or described implicitly by (3.6a, b) or (3.7a, b). Each three-dimensional manifold $\mathcal{W}(O^L)$ is the intersection of the four-dimensional manifold $\mathcal{W}(\Pi)$ with one of the five-dimensional manifolds $\mathcal{M}^L = \{(x,u,v)|L(x,u,v) = \text{constant}\}$ in the six-dimensional phase space. Moreover, each manifold $\mathcal{W}(O^L)$ is the intersection of $\mathcal{W}(\Pi)$ with the five-dimensional manifold $\mathcal{M}^H = \{(x,u,v)|H(x,u,v) = \text{constant}\}$, where the constants in the definitions of $\mathcal{M}^H$ and $\mathcal{M}^L$ are connected by the relation $H = 2\omega L$. (This relation follows from (3.6a) and (3.6b).) Thus, each homoclinic manifold $\mathcal{W}(O^L)$ lies inside a unique four-dimensional manifold $\mathcal{M}^{H,L} = \{(x,u,v)|H(x,u,v) = \text{constant}, \ L(x,u,v) = \text{constant}\}$, where the constants are connected by the relation $H = 2\omega L$. This geometry is sketched in fig. 5.

4. Persistence of invariant manifolds

We now investigate persistence under the ϵ-perturbation of the structures described in the previous section. This investigation is facilitated by conservation of L and its associated phase symmetry remaining under the perturbation. We proceed by using yet another canonical transformation to separate out the action–angle pair, L and its conjugate phase angle. This separation reduces the perturbed equations to a form in which persistence of the periodic orbits and their stable and unstable manifolds discussed in the previous section may be proven with elementary methods, such as the implicit function theorem and the usual stable manifold theorem (see refs. [17, 18]).

We begin by performing the canonical coordinate change

$$x = x, \quad u = \sqrt{2L - |z|^2}\, e^{i\varphi}, \quad v = z\, e^{i\varphi},$$

valid for $|z|^2 < 2L$. (Again, there is a singularity in these coordinates akin to that for planar polar coordinates at the origin.) The Hamiltonian H in these coordinates is

$$H = 2\omega L + \tfrac{1}{2}\omega|x-\epsilon|^2 - \tfrac{1}{2}\omega|z|^2 - \tfrac{1}{2}\sqrt{2L-|z|^2}\,(xz + x^*z^*), \qquad (4.1)$$

and the new symplectic form is $-(1/2i)(dx \wedge dx^* + dz \wedge dz^*) + dL \wedge d\varphi$. The equations for

x and z decouple from those for L and φ, and become

$$\dot{x} = -i\omega(x-\epsilon) + i\sqrt{2L-|z|^2}\,z^*, \tag{4.2a}$$

$$\dot{z} = i\omega z + i\sqrt{2L-|z|^2}\,x^* - \frac{i}{2}\frac{z}{\sqrt{2L-|z|^2}}(xz + x^*z^*). \tag{4.2b}$$

For $\epsilon = 0$, the point P_0 at the origin $x = z = 0$ is a fixed point of this system, whose linearized equations are

$$\dot{x} = -i\omega x + i\sqrt{2L}\,z^*, \quad \dot{z} = i\omega z + i\sqrt{2L}\,x^*.$$

The stability matrix of this equilibrium at the origin is thus

$$\begin{pmatrix} 0 & \omega & 0 & \sqrt{2L} \\ -\omega & 0 & \sqrt{2L} & 0 \\ 0 & \sqrt{2L} & 0 & -\omega \\ \sqrt{2L} & 0 & \omega & 0 \end{pmatrix}. \tag{4.3}$$

The eigenvalues of this stability matrix are $\pm(\sqrt{2L} \pm i\omega)$. Therefore, the origin P_0 is a hyperbolic fixed point of the system (4.2). (In fact, it is a spiral–saddle with two unstable and two stable directions.) Returning to the (x, u, v) coordinates, we see that the (x, z) origin P_0 corresponds precisely to the periodic orbit O^L in the u-plane Π.

By the implicit function theorem, a fixed point near the origin of the (x, z) coordinates persists in (4.2) for small but nonzero ϵ. Moreover, this perturbed fixed point, P_ϵ^L, is still hyperbolic, and, therefore, it possesses two-dimensional stable, and two-dimensional unstable manifolds, $\mathscr{W}^s(P_\epsilon^L)$ and $\mathscr{W}^u(P_\epsilon^L)$, respectively. The orbits on these manifolds spiral as they approach, or depart from, the perturbed fixed point P_ϵ^L, due to the form of the eigenvalues of the linearized problem. The perturbed fixed point P_ϵ^L together with its stable and unstable manifolds $\mathscr{W}^s(P_\epsilon^L)$ and $\mathscr{W}^u(P_\epsilon^L)$ also varies smoothly with L.

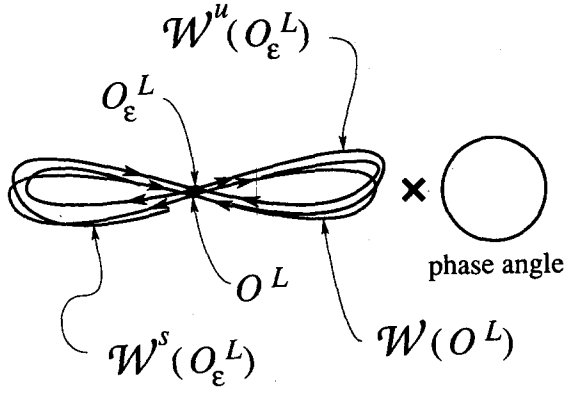

Fig. 6. The perturbed periodic orbit O_ϵ^L possesses smooth, three-dimensional stable and unstable manifolds, $\mathscr{W}^s(O_\epsilon^L)$ and $\mathscr{W}^u(O_\epsilon^L)$, which both limit on the unperturbed homoclinic manifold $\mathscr{W}(O^L)$ as $\epsilon \to 0$.

To reconstruct the full solution, we add the angle φ back into the picture via a quadrature. Thus, the fixed point for the perturbed equations (4.2) becomes a periodic orbit O_ϵ^L for the original equations (2.2). This perturbed periodic orbit possesses smooth three-dimensional stable and unstable manifolds, denoted $\mathscr{W}^s(O_\epsilon^L)$ and $\mathscr{W}^u(O_\epsilon^L)$, respectively, both of which limit on $\mathscr{W}(O^L)$ as $\epsilon \to 0$. (See fig. 6.) The frequency of the periodic orbit O_ϵ^L is $-\partial H/\partial L = -2\omega + \epsilon f(L, \epsilon)$, where f is a smooth function of L and ϵ, determined by evaluating the derivative $\partial H/\partial L$ at the perturbed fixed point P_ϵ^L. The orbit O_ϵ^L, together with its stable and unstable manifolds $\mathscr{W}^s(O_\epsilon^L)$ and $\mathscr{W}^u(O_\epsilon^L)$, lies inside the perturbed manifold $\mathscr{M}_\epsilon^{H,L}$, on which H and L are connected by the smooth functional relation $H = h(L, \epsilon)$, with $h(L, 0) = 2\omega L$. The precise form of the function $h(L, \epsilon)$ for nonzero ϵ may be obtained by inserting the values of x and z at the perturbed hyperbolic equilibrium P_ϵ^L into the Hamiltonian (4.1).

The union of the perturbed periodic orbits O_ϵ^L is a two-dimensional surface Π_ϵ, parametrized by L and φ, and lying $\mathscr{O}(\epsilon)$ close to the unperturbed u-plane Π. Stable and unstable manifolds $\mathscr{W}^s(O_\epsilon^L)$ and $\mathscr{W}^u(O_\epsilon^L)$ of the perturbed periodic orbits O_ϵ^L in Π_ϵ form two smooth four-dimen-

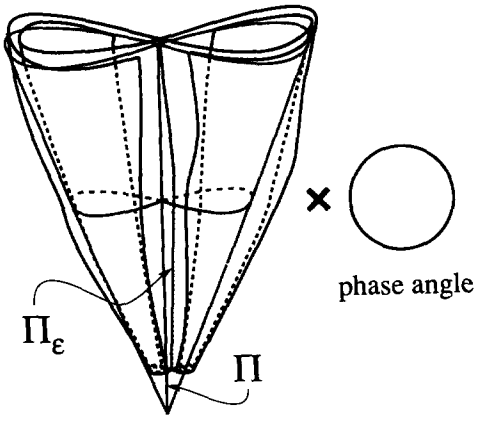

Fig. 7. The union of the stable and unstable manifolds $\mathscr{W}^s(O_\epsilon L)$ and $\mathscr{W}^u(O_\epsilon^L)$ of the perturbed periodic orbits O_ϵ^L form two smooth four-dimensional manifolds, $\mathscr{W}^s(\Pi_\epsilon)$ and $\mathscr{W}^u(\Pi_\epsilon)$, lying near the union of the unperturbed homoclinic manifolds, $\mathscr{W}(\Pi)$.

sional manifolds, $\mathscr{W}^s(\Pi_\epsilon)$ and $\mathscr{W}^u(\Pi_\epsilon)$, which both limit on $\mathscr{W}(\Pi)$ for $\epsilon \to 0$. (See fig. 7.)

We cannot expect the manifolds $\mathscr{W}^s(\Pi_\epsilon)$ and $\mathscr{W}^u(\Pi_\epsilon)$, and even less the smaller-dimensional manifolds $\mathscr{W}^s(O_\epsilon^L)$ and $\mathscr{W}^u(O_\epsilon^L)$, to coincide for nonzero ϵ as they did for $\epsilon = 0$. However, they may intersect along subsets of smaller dimension. Such intersections may give rise to interesting behavior, including chaos. We investigate the criteria for $\mathscr{W}^s(O_\epsilon^L)$ and $\mathscr{W}^u(O_\epsilon^L)$ to intersect in the next section.

5. Homoclinic intersections of invariant manifolds

In this section, we use the Melnikov method [19–27], in order to investigate the intersections of the stable and the unstable manifolds, $\mathscr{W}^s(O_\epsilon^L)$ and $\mathscr{W}^u(O_\epsilon^L)$, of the perturbed periodic orbits O_ϵ^L in the perturbed surface Π_ϵ. This method consists of computing an approximate distance between pairs of points on the manifolds $\mathscr{W}^s(O_\epsilon^L)$ and $\mathscr{W}^u(O_\epsilon^L)$, and concluding by using the implicit function theorem that, near points where this approximate distance vanishes, so must the true distance. At those points, the manifolds $\mathscr{W}^s(O_\epsilon^L)$ and $\mathscr{W}^u(O_\epsilon^L)$ intersect.

We must, therefore, locate pairs of points on $\mathscr{W}^s(O_\epsilon^L)$ and $\mathscr{W}^u(O_\epsilon^L)$, between which we will compute the distance. First, we parametrize the perturbed manifolds $\mathscr{W}^s(O_\epsilon^L)$ and $\mathscr{W}^u(O_\epsilon^L)$ by using the unperturbed homoclinic manifold $\mathscr{W}(O^L)$ to provide the proper coordinate chart. The unperturbed manifold $\mathscr{W}(O^L)$ is parametrized by the coordinates t, ψ_0 and θ_0, via expression (3.5) for the homoclinic solutions. To each point a in the unperturbed manifold $\mathscr{W}(O^L)$, we assign a unique point a_ϵ^s in the perturbed stable manifold $\mathscr{W}^s(O_\epsilon^L)$ and a unique point a_ϵ^u in the perturbed unstable manifold $\mathscr{W}^u(O_\epsilon^L)$ in the following way. We consider the normal space Σ_a to the unperturbed manifold $\mathscr{W}(O^L)$ at a. Since $\mathscr{W}(O^L)$ is implicitly described by eqs. (3.6), every vector in the normal space Σ_a is a linear combination of the three independent normals to the unperturbed manifold $\mathscr{W}(O^L)$, which can be computed from (3.6). These three normals are

$$\boldsymbol{n}_1 = \omega\nabla L + \omega\nabla J - \nabla H, \quad \boldsymbol{n}_2 = \nabla J - \nabla L,$$
$$\boldsymbol{n}_3 = \nabla L.$$

By construction, in a small enough neighborhood of a, the normal space Σ_a intersects the unperturbed manifold $\mathscr{W}(O^L)$ transversely in precisely the point a. Since transverse intersections survive small perturbations, the normal space Σ_a also intersects the perturbed manifolds $\mathscr{W}^s(O_\epsilon^L)$ and $\mathscr{W}^u(O_\epsilon^L)$ transversely in at least one discrete point each. Of all the intersection points of Σ_a and the stable manifold $\mathscr{W}^s(O_\epsilon^L)$ inside a small enough neighborhood of the point a, we choose a_ϵ^s to be the one that takes the least amount of time to reach any arbitrarily small neighborhood of the periodic orbit O_ϵ^L. Likewise, we choose a_ϵ^u to be the point of intersection of Σ_a and the unstable manifold $\mathscr{W}^u(O_\epsilon^L)$ that takes the least amount of time going backward to reach any arbitrarily small neighborhood of O_ϵ^L. (The choice of the points a_ϵ^s and a_ϵ^u is sketched in fig. 8.) At each point a in

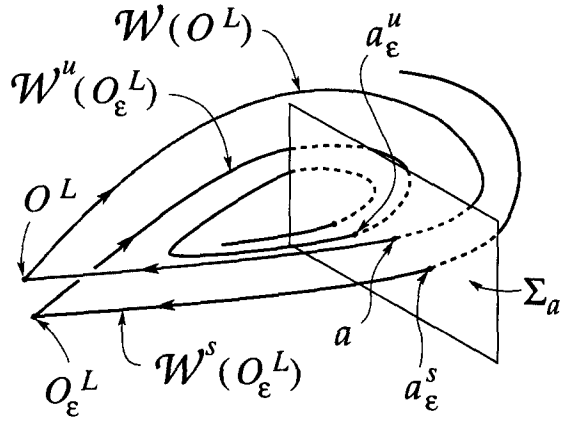

Fig. 8. The unperturbed homoclinic manifold $\mathcal{W}(O^L)$ pierces the normal space Σ_a at the point a. The perturbed stable and unstable manifolds $\mathcal{W}^s(O_\epsilon^L)$ and $\mathcal{W}^u(O_\epsilon^L)$ pierce Σ_a near the point a at the points a_ϵ^s and a_ϵ^u.

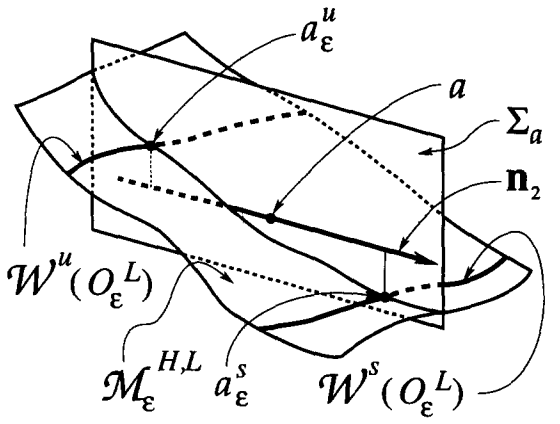

Fig. 9. The points a_ϵ^s and a_ϵ^u lie on the same level surface $\mathcal{M}_\epsilon^{H,L}$. Therefore, only one component of the vector $a_\epsilon^u - a_\epsilon^s$ needs to be calculated in order to determine when this vector vanishes. When the vector $a_\epsilon^u - a_\epsilon^s$ vanishes, the perturbed stable and unstable manifolds $\mathcal{W}^s(O_\epsilon^L)$ and $\mathcal{W}^u(O_\epsilon^L)$ intersect.

the unperturbed manifold $\mathcal{W}(O^L)$, we use the difference between the corresponding points a_ϵ^s and a_ϵ^u (that is, the vector $a_\epsilon^u - a_\epsilon^s$) in order to compute the distance between the stable and unstable manifolds $\mathcal{W}^s(O_\epsilon^L)$ and $\mathcal{W}^u(O_\epsilon^L)$. In particular, if the vector $a_\epsilon^u - a_\epsilon^s$ vanishes, the manifolds $\mathcal{W}^s(O_\epsilon^L)$ and $\mathcal{W}^u(O_\epsilon^L)$ intersect at the point $a_\epsilon^s = a_\epsilon^u$.

At first, it seems that one must compute all three components of the vector $a_\epsilon^u - a_\epsilon^s$, along $\boldsymbol{n}_1$, $\boldsymbol{n}_2$ and $\boldsymbol{n}_3$, in order to establish intersection of the manifolds $\mathcal{W}^s(O_\epsilon^L)$ and $\mathcal{W}^u(O_\epsilon^L)$. However, one should remember that both H and L are constants of motion, even for nonzero ϵ. This means that both $\mathcal{W}^s(O_\epsilon^L)$ and $\mathcal{W}^u(O_\epsilon^L)$ are contained in the same manifold $\mathcal{M}_\epsilon^{H,L}$. Moreover, this manifold $\mathcal{M}_\epsilon^{H,L}$ is transverse to the normal space Σ_a to the unperturbed homoclinic manifold $\mathcal{W}(O^L)$ at the point a, since its two normals ∇H and ∇L are contained in the normal space Σ_a, at least for $\epsilon = 0$. Therefore, we conclude that $\mathcal{M}_\epsilon^{H,L}$ and Σ_a intersect transversely near a along a curve, which contains both the points a_ϵ^s and a_ϵ^u. This geometrical fact implies two functional relations among the three components of the vector $a_\epsilon^u - a_\epsilon^s$, and hence only one of the three components needs to be calculated in order to establish that the manifolds $\mathcal{W}^s(O_\epsilon^L)$ and $\mathcal{W}^u(O_\epsilon^L)$ intersect. (See fig. 9.)

We choose to compute the component of the vector $a_\epsilon^u - a_\epsilon^s$ along the normal $\boldsymbol{n}_2$. The component along $\boldsymbol{n}_2$ is equal to

$$d(a,\epsilon) = \frac{\langle a_\epsilon^u - a_\epsilon^s, \boldsymbol{n}_2(a)\rangle}{\|\boldsymbol{n}_2(a)\|},$$

where $\langle \cdot, \cdot \rangle$ denotes the usual scalar product in $\mathbb{R}^6$ and $\|\cdot\|$ is the corresponding norm. The numerator can be Taylor expanded (see refs. [25, 27]) to become

$$\langle a_\epsilon^u - a_\epsilon^s, \boldsymbol{n}_2(a)\rangle = \epsilon M(L;\psi_0,\theta_0;\omega) + \mathcal{O}(\epsilon^2).$$

The expression

$$M(L;\psi_0,\theta_0;\omega) = \int_{-\infty}^{\infty} \langle \boldsymbol{n}_2(a(t)), \boldsymbol{g}(a(t))\rangle \, dt$$

is called the Melnikov function, and is evaluated along the unique unperturbed homoclinic solution $a(t)$, given by expressions (3.5) and passing through the point a. The vector $\boldsymbol{g}$ is the $\mathcal{O}(\epsilon)$ perturbation part of the vector field (2.2). In components, we have

$$\boldsymbol{n}_2 = (x_1, x_2, 0, 0, -v_1, -v_2)$$

and

$$g = (0, \omega, 0, 0, 0, 0).$$

We therefore compute the Melnikov function to be

$$\begin{aligned} M(L; \psi_0, \theta_0; \omega) &= \omega \int_{-\infty}^{\infty} x_2(a(t))\, dt \\ &= \omega\sqrt{2L} \int_{-\infty}^{\infty} \operatorname{sech}(\sqrt{2L}\, t) \sin(-\omega t + \psi_0)\, dt \\ &= \pi\omega \operatorname{sech}\left(\frac{\pi\omega}{2\sqrt{2L}}\right) \sin\psi_0. \end{aligned} \tag{5.1}$$

Note that the Melnikov function depends on neither t nor θ_0. The fact that it does not depend on t (even though each individual point a does) means that the function $M(L; \psi_0, \theta_0; \omega)$ is constant along the unperturbed homoclinic orbits. In particular, if $M(L; \psi_0, \theta_0; \omega)$ vanishes at some point a, it will vanish along the whole homoclinic orbit parametrized by $a(t)$. This was to be expected because of the invariance of the manifolds $\mathcal{W}^s(O_\epsilon^L)$ and $\mathcal{W}^u(O_\epsilon^L)$; namely, if $\mathcal{W}^s(O_\epsilon^L)$ and $\mathcal{W}^u(O_\epsilon^L)$ intersect in a point, they must intersect along the whole orbit passing through this point. The fact that the function $M(L; \psi_0, \theta_0; \omega)$ does not depend on θ_0 is a consequence of the rotational symmetry of the perturbed Hamiltonian (2.3) with respect to the angle θ_0 and the corresponding conservation of L.

The Melnikov function $M(L; \psi_0, \theta_0; \omega)$ in (5.1) has simple zeros at $\psi_0 = 0$ and $\psi_0 = \pi$. By using the implicit function theorem on the distance function $d(a, \epsilon)/\epsilon$, we immediately conclude that the manifolds $\mathcal{W}^s(O_\epsilon^L)$ and $\mathcal{W}^u(O_\epsilon^L)$ intersect in the normal space Σ_a at every point a coordinatized by an unperturbed homoclinic solution (3.5) for which $\psi_0 = 0$ or $\psi_0 = \pi$. Keeping in mind that the quantity L is fixed on the manifolds $\mathcal{W}^s(O_\epsilon^L)$ and $\mathcal{W}^u(O_\epsilon^L)$, we find that the three-dimensional manifolds $\mathcal{W}^s(O_\epsilon^L)$ and $\mathcal{W}^u(O_\epsilon^L)$ intersect along two two-dimensional surfaces, parametrized by t and θ_0 in the solutions (3.5) with $\psi_0 = 0$ and $\psi_0 = \pi$. We address transversality of these intersections in the next section.

6. Transversality of homoclinic intersections

In this section we discuss transversality of the intersections of the perturbed manifolds $\mathcal{W}^s(O_\epsilon^L)$ and $\mathcal{W}^u(O_\epsilon^L)$ inside the manifold $\mathcal{M}_\epsilon^{H,L}$. (See refs. [24, 26, 27].) We begin by recalling that both $\mathcal{W}^s(O_\epsilon^L)$ and $\mathcal{W}^u(O_\epsilon^L)$ are three-dimensional, their intersections are two-dimensional and the manifold $\mathcal{M}_\epsilon^{H,L}$ is four-dimensional. The rule that the dimension of the transverse intersection of two manifolds inside the third one equals the sum of the dimensions of the intersecting manifolds, minus the dimension of the ambient manifold, leads us to the conjecture that the intersections of $\mathcal{W}^s(O_\epsilon^L)$ and $\mathcal{W}^u(O_\epsilon^L)$ inside $\mathcal{M}_\epsilon^{H,L}$ should be transverse. However, this rule is only a necessary criterion for transversality, and therefore, we must still prove the conjecture.

To prove the transversality of the intersections of the stable and unstable manifolds $\mathcal{W}^s(O_\epsilon^L)$ and $\mathcal{W}^u(O_\epsilon^L)$ of the perturbed periodic orbits O_ϵ^L inside the manifold $\mathcal{M}_\epsilon^{H,L}$, we must show that at any intersection point $a_\epsilon^s = a_\epsilon^u$, the tangent spaces $T\mathcal{W}^s(O_\epsilon^L)$ and $T\mathcal{W}^u(O_\epsilon^L)$ of the intersecting manifolds $\mathcal{W}^s(O_\epsilon^L)$ and $\mathcal{W}^u(O_\epsilon^L)$, respectively, add up to the tangent space $T\mathcal{M}_\epsilon^{H,L}$ of the level manifold $\mathcal{M}_\epsilon^{H,L}$ at $a_\epsilon^s = a_\epsilon^u$. We show this by explicitly computing the respective bases of the tangent spaces $T\mathcal{W}^s(O_\epsilon^L)$ and $T\mathcal{W}^u(O_\epsilon^L)$ at the intersection point $a_\epsilon^s = a_\epsilon^u$, and showing that we can pick a basis of the tangent space $T\mathcal{M}_\epsilon^{H,L}$ from among their linear combinations. We also show the reason that we can combine the bases of $T\mathcal{W}^s(O_\epsilon^L)$ and $T\mathcal{W}^u(O_\epsilon^L)$ into a basis of $T\mathcal{M}_\epsilon^{H,L}$ to be that the zeros in ψ_0 of the Melnikov function $M(L; \psi_0, \theta_0; \omega)$ are simple.

We begin by noting that the three vectors $\partial a/\partial t$, $\partial a/\partial\psi_0$ and $\partial a/\partial\theta_0$, which can be calculated from the homoclinic solution (3.5), span the tangent space $T\mathcal{W}(O^L)$ of the unperturbed ho-

moclinic manifold $\mathscr{W}(O^L)$ at the point a. Since $\mathscr{W}(O^L)$ is contained in one of the manifolds $\mathscr{M}^{H,L}$, the same inclusion holds for the respective tangent spaces. Now, the tangent space $T\mathscr{M}^{H,L}$ of $\mathscr{M}^{H,L}$ at the point a is four-dimensional, so we need to add one more linearly-independent vector to the set $\partial a/\partial t$, $\partial a/\partial\psi_0$ and $\partial a/\partial\theta_0$, in order to find a basis for $T\mathscr{M}^{H,L}$ at the point a. A suitable additional vector is the projection $\tilde{n}_2$ of the normal n_2 onto $T\mathscr{M}^{H,L}$, given by

$$\tilde{n}_2 = n_2 - \frac{\langle n_2, \nabla L\rangle}{\|\nabla L\|^2}\nabla L - \frac{\langle n_2, \nabla H\rangle}{\|\nabla H\|^2}\nabla H.$$

This vector is nonzero because $n_2 = \nabla J - \nabla L$, and the gradients ∇H, ∇L and ∇J are linearly independent. Also, since n_2 is normal to the vectors $\partial a/\partial t$, $\partial a/\partial\psi_0$ and $\partial a/\partial\theta_0$, its projection $\tilde{n}_2$ is transverse to them.

When ϵ is nonzero, the tangent spaces $T\mathscr{W}^s(O_\epsilon^L)$ and $T\mathscr{W}^u(O_\epsilon^L)$ at the points a_ϵ^s and a_ϵ^u, respectively, are spanned by the two triples of vectors

$$\frac{\partial a_\epsilon^s}{\partial t},\ \frac{\partial a_\epsilon^s}{\partial\psi_0},\ \frac{\partial a_\epsilon^s}{\partial\theta_0},\ \text{and}\ \frac{\partial a_\epsilon^u}{\partial t},\ \frac{\partial a_\epsilon^u}{\partial\psi_0},\ \frac{\partial a_\epsilon^u}{\partial\theta_0}. \tag{6.1}$$

All these vectors are contained in the perturbed tangent spaces $T\mathscr{M}_\epsilon^{H,L}$ at their respective base points a_ϵ^s and a_ϵ^u. Moreover, if these points coincide so that $a_\epsilon^s = a_\epsilon^u$, the vectors (6.1), which now lie in the same tangent space $T\mathscr{M}_\epsilon^{H,L}$, are still transverse to the projection $\tilde{n}_{2,\epsilon}$ of the normal n_2 onto the perturbed tangent space $T\mathscr{M}_\epsilon^{H,L}$ to the manifold $\mathscr{M}_\epsilon^{H,L}$ at the point $a_\epsilon^s = a_\epsilon^u$. Therefore, if we find any linear combination of the six vectors (6.1) which has a nonzero projection along $\tilde{n}_{2,\epsilon}$, then these six vectors span the perturbed tangent space $T\mathscr{M}_\epsilon^{H,L}$. This last statement is equivalent to saying that $\mathscr{W}^s(O_\epsilon^L)$ and $\mathscr{W}^u(O_\epsilon^L)$ intersect transversely inside the manifold $\mathscr{M}_\epsilon^{H,L}$ at the point $a_\epsilon^s = a_\epsilon^u$.

Now, any linear combination of the vectors (6.1) is contained in the tangent space $T\mathscr{M}_\epsilon^{H,L}$ at

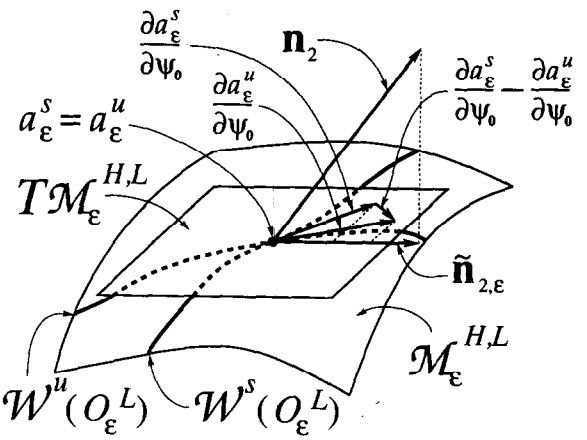

Fig. 10. The intersection of the perturbed stable and unstable manifolds $\mathscr{W}^s(O_\epsilon^L)$ and $\mathscr{W}^u(O_\epsilon^L)$ is transverse when the vector $\partial a_\epsilon^u/\partial\psi_0 - \partial a_\epsilon^s/\partial\psi_0$ has a nonzero projection onto the vector $\tilde{n}_{2,\epsilon}$, or equivalently, onto the vector n_2.

$a_\epsilon^s = a_\epsilon^u$. The normal n_2 can be written as $n_2 = \tilde{n}_{2,\epsilon} + (n_2 - \tilde{n}_{2,\epsilon})$, where $\tilde{n}_{2,\epsilon}$ is contained in $T\mathscr{M}_\epsilon^{H,L}$ and the difference $(n_2 - \tilde{n}_{2,\epsilon})$ is contained in its orthogonal complement. It follows that the scalar product of any linear combination of vectors (6.1) with $\tilde{n}_{2,\epsilon}$ is the same as the scalar product of that linear combination with n_2, because the vectors (6.1) are contained in $T\mathscr{M}_\epsilon^{H,L}$.

Therefore, to prove transversality of the intersection of $\mathscr{W}^s(O_\epsilon^L)$ and $\mathscr{W}^u(O_\epsilon^L)$ inside $\mathscr{M}_\epsilon^{H,L}$ at the point $a_\epsilon^u = a_\epsilon^s$, we need only find a linear combination of vectors (6.1) whose scalar product with n_2 is nonzero. One such linear combination is the vector $\partial a_\epsilon^u/\partial\psi_0 - \partial a_\epsilon^s/\partial\psi_0$. (See fig. 10.) Since $a_\epsilon^s = a_\epsilon^u$ at our intersection point, this statement follows from the following calculation:

$$\begin{aligned}
&\left\langle \frac{\partial a_\epsilon^u}{\partial\psi_0} - \frac{\partial a_\epsilon^s}{\partial\psi_0}, n_2 \right\rangle \\
&= \left\langle \frac{\partial a_\epsilon^u}{\partial\psi_0} - \frac{\partial a_\epsilon^s}{\partial\psi_0}, n_2 \right\rangle + \left\langle a_\epsilon^u - a_\epsilon^s, \frac{\partial n_2}{\partial\psi_0} \right\rangle \\
&= \frac{\partial\langle a_\epsilon^u - a_\epsilon^s, n_2\rangle}{\partial\psi_0} \\
&= \epsilon\frac{\partial M(L;\psi_0,\theta_0;\omega)}{\partial\psi_0} + \mathscr{O}(\epsilon^2),
\end{aligned}$$

evaluated at $\psi_0 = 0$ or $\psi_0 = \pi$, according to the results found in the previous section. By (5.1) in the previous section, we have an expression for the Melnikov function,

$$M(L;\psi_0,\theta_0;\omega) = \pi\omega \operatorname{sech}\left(\frac{\pi\omega}{2\sqrt{2L}}\right)\sin\psi_0.$$

Therefore, the projection under consideration,

$$\left\langle \frac{\partial a_\epsilon^u}{\partial\psi_0} - \frac{\partial a_\epsilon^s}{\partial\psi_0}, \boldsymbol{n}_2 \right\rangle = \pm\epsilon\pi\omega \operatorname{sech}\left(\frac{\pi\omega}{2\sqrt{2L}}\right) + \mathcal{O}(\epsilon^2),$$

is nonzero for small enough ϵ.

In summary, since the derivative $\partial M(L;\psi_0,\theta_0;\omega)/\partial\psi_0$ of the Melnikov function is nonzero at the intersection points, $\psi_0 = 0$ and $\psi_0 = \pi$, the perturbed stable and unstable manifolds $\mathscr{W}^s(O_\epsilon^L)$ and $\mathscr{W}^u(O_\epsilon^L)$ of the periodic orbit O_ϵ^L intersect transversely inside the corresponding level manifold $\mathscr{M}_\epsilon^{H,L}$.

7. Small detuning

In this section we briefly discuss the second near-integrable limit of the Maxwell–Schrödinger envelope equations, namely, the one in which the laser probe is nearly frequency-matched with the resonant medium so that the dimensionless detuning ω is small, $\omega \ll 1$[#3]. The unperturbed ($\omega = 0$) version of this system is

$$\dot{x} = \mathrm{i}uv^*, \tag{7.1a}$$

$$\dot{u} = \mathrm{i}xv, \tag{7.1b}$$

$$\dot{v} = \mathrm{i}x^*u. \tag{7.1c}$$

This system can be derived from the Hamiltonian

$$H = -\tfrac{1}{2}xu^*v - \tfrac{1}{2}x^*uv^*,$$

using the complex symplectic form $-(1/2\mathrm{i})(\mathrm{d}x\wedge\mathrm{d}x^* + \mathrm{d}u\wedge\mathrm{d}u^* + \mathrm{d}v\wedge\mathrm{d}v^*)$. System (7.1) is a special case of eqs. (3.1) with $\omega = 0$. Therefore, the analysis in section 3 can be specialized here to give the homoclinic solutions (cf. eqs. (3.5))

$$x = \sqrt{2L}\,\operatorname{sech}(\sqrt{2L}\,t)\,\mathrm{e}^{\mathrm{i}\psi_0}, \tag{7.2a}$$

$$u = \mathrm{i}\sqrt{2L}\,\tanh(\sqrt{2L}\,t)\,\mathrm{e}^{\mathrm{i}(\psi_0+\theta_0)}, \tag{7.2b}$$

$$v = \sqrt{2L}\,\operatorname{sech}(\sqrt{2L}\,t)\,\mathrm{e}^{\mathrm{i}\theta_0}. \tag{7.2c}$$

As already mentioned in section 3, these solutions connect antipodal points on the circle O^L of radius $\sqrt{2L}$ in the complex u-plane Π. The corresponding homoclinic manifold $\mathscr{W}(O^L)$ can now either be parametrized by expressions (7.2), or it can be described implicitly by the equations

$$H = 0, \tag{7.3a}$$

$$J - L = 0, \tag{7.3b}$$

$$L = \text{constant}, \tag{7.3c}$$

whose left-hand sides are identical to the left-hand sides of eqs. (3.7). The geometry of the homoclinic manifolds $\mathscr{W}(O^L)$ and their union $\mathscr{W}(\Pi)$ is the same as the geometry of their counterparts in section 3.

Persistence of these structures under the perturbation may be shown in the same way as in section 4. In particular, one may again transform the perturbed Hamiltonian into the form (4.1), that is,

$$H = 2\omega L + \tfrac{1}{2}\omega|x-\epsilon|^2 - \tfrac{1}{2}\omega|z|^2 - \tfrac{1}{2}\sqrt{2L-|z|^2}\,(xz + x^*z^*),$$

and the nontrivial part of the equations into (4.2), that is,

$$\dot{x} = -\mathrm{i}\omega(x-\epsilon) + \mathrm{i}\sqrt{2L-|z|^2}\,z^*,$$

$$\dot{z} = \mathrm{i}\omega z + \mathrm{i}\sqrt{2L-|z|^2}\,x^* - \frac{\mathrm{i}}{2}\frac{z}{\sqrt{2L-|z|^2}}(xz + x^*z^*),$$

[#3] Dimensionally, this means that the detuning is small compared to the cooperative frequency ω_c, given in section 2.

where ω is now the perturbation parameter. For $\omega = 0$, the eigenvalues of the corresponding linearization of eqs. (4.2) around the origin are two degenerate pairs of $\pm\sqrt{2L}$. For this form of the eigenvalues, the implicit function theorem and the stable manifold theorem again imply that the equilibrium at the origin of the reduced system (4.2) persists under the perturbation (which is now comprised of the ω-terms) together with its stable and its unstable manifolds, and that they all vary smoothly with L.

At this point, however, we must take a slight digression from the treatment in section 4. Specifically, we must as an extra step determine whether the linearized eigenvalues of the perturbed equilibrium have nonzero imaginary parts, implying that the equilibrium is a spiral–saddle. We must also determine whether the perturbed equilibrium in the reduced phase space corresponds to a periodic orbit, or to a ring of equilibria in the full phase space. We first calculate the lowest-order terms in the Taylor expansions of the position of the perturbed equilibrium and of its eigenvalues. Setting the left-hand sides of eqs. (4.2) equal to zero implies, after some algebra, that

$$x = \mathcal{O}(\omega^2), \quad z = -\frac{\omega\epsilon}{\sqrt{2L}} + \mathcal{O}(\omega^2).$$

Additional algebra shows that the lowest-order approximation of the stability matrix at the perturbed equilibrium is just the matrix (4.3), that is

$$\begin{pmatrix} 0 & \omega & 0 & \sqrt{2L} \\ -\omega & 0 & \sqrt{2L} & 0 \\ 0 & \sqrt{2L} & 0 & -\omega \\ \sqrt{2L} & 0 & \omega & 0 \end{pmatrix}.$$

The corresponding perturbed eigenvalues are equal to $\pm\{\sqrt{2L} + \mathcal{O}(\omega) \pm i\omega[1 + \mathcal{O}(\omega)]\}$, where the $\mathcal{O}(\omega)$ quantities are real. (Due to the Hamiltonian nature of the problem, the eigenvalues come in a "quartet".) Thus, we see that orbits on the stable and the unstable manifolds of the perturbed equilibrium are again spirals just as in section 4; however, their twisting rate is now very slow. The quadrature equation for the angle φ at the perturbed equilibrium now is

$$\dot{\varphi} = -2\omega + \mathcal{O}(\omega^3).$$

Therefore, this perturbed equilibrium in the reduced phase space corresponds to a periodic orbit in the full phase space whose frequency is very low.

The rest of the analysis follows as in the case of small amplitude ϵ. In particular, one may use the Melnikov method in order to show that transverse intersections of the stable and the unstable manifolds, $\mathcal{W}^s(O_\omega^L)$ and $\mathcal{W}^u(O_\omega^L)$, of the perturbed periodic orbit O_ω^L take place on the corresponding perturbed level surface $\mathcal{M}_\omega^{H,L}$.

Explicitly, the Melnikov function for the small ω case is

$$M(L;\psi_0,\theta_0;\epsilon) = \int_{-\infty}^{\infty} \langle \boldsymbol{n}_2(a(t)), \boldsymbol{g}(a(t)) \rangle \, dt,$$

where $\boldsymbol{g}$ now is the $\mathcal{O}(\omega)$ part of the vector field (2.2), that is,

$$\boldsymbol{g} = (x_2, -x_1 + \epsilon, u_2, -u_1, v_2, -v_1).$$

The Melnikov function thus turns out to be

$$M(L;\psi_0,\theta_0;\epsilon) = \epsilon \int_{-\infty}^{\infty} x_2(a(t)) \, dt$$

$$= \epsilon\sqrt{2L}\sin\psi_0 \int_{-\infty}^{\infty} \operatorname{sech}(\sqrt{2L}\, t) \, dt = \pi\epsilon\sin\psi_0.$$

As in section 5, this function has transverse zeros at $\psi_0 = 0$ and $\psi_0 = \pi$. Therefore, the geometry of the transverse intersections caused by the probe laser in the case of small detuning, ω, is the same as in the case of small amplitude, ϵ. Hence, the Smale horseshoe construction presented in the next section will be the same for both types of perturbations.

8. Smale horseshoe and chaotic dynamics

The Melnikov analysis presented in the previous three sections shows that the stable and unstable manifolds of the hyperbolic periodic orbits O^L develop transverse intersections under the perturbations introduced by the probe laser. (For definiteness, we refer in this section only to the ϵ-perturbation case. The ω-perturbation case follows along the same lines.) These transverse intersections take place in $\mathbb{C}^3$ (with coordinates (x, u, v)) and lie on the level surfaces $\mathcal{M}_\epsilon^{H,L}$. We show in this section, by extending a result of Devaney [16], that this presence of transverse intersections implies chaotic dynamics for phase points in the vicinity of these intersections.

Devaney [16] treats the case of an autonomous two-degree-of-freedom Hamiltonian system whose phase space is $\mathbb{C}^2$. In Devaney's case, transverse intersections of the two-dimensional stable and unstable manifolds of a spiral–saddle fixed point form a single, one-dimensional, Hamiltonian, spiral–saddle connection orbit in the three-dimensional level surface of the constant Hamiltonian that contains the spiral–saddle fixed point. In order to show that chaos results from this Hamiltonian spiral–saddle connection orbit, Devaney constructs a return map, Φ, defined in the phase space $\mathbb{C}^2$ by composing two maps, Φ_0 and Φ_1. The first map, Φ_0, is defined locally near the fixed point. This map pushes a set of phase points that is initially close to the spiral–saddle fixed point (and lies on a small two-dimensional surface transverse to the flow near the *stable* manifold of the fixed point) to a set of phase points that lies on another surface close to the fixed point and is transverse to the flow near its *unstable* manifold. The second map, Φ_1, is the global part of the return map Φ. The map Φ_1 takes the result of the first map Φ_0 back around the homoclinic orbit into the region of the first set of initial phase points. Devaney [16] shows that iteration of the return map Φ, that is, the composition map $\Phi_1 \circ \Phi_0$, produces an invariant Cantor set of points on which the dynamics are equivalent to a Bernoulli shift on two symbols. Thus, one-dimensional transverse intersections in $\mathbb{C}^2$ forming a Hamiltonian spiral–saddle connection orbit result in chaotic dynamics via sensitivity to initial conditions for phase points in the vicinity of these intersections.

The Maxwell–Schrödinger problem we treat differs from Devaney's case in having $\mathbb{C}^3$ as its phase space instead of $\mathbb{C}^2$, and in having hyperbolic periodic orbits instead of a spiral–saddle fixed point. However, the Maxwell–Schrödinger problem does have the extra conserved quantity L. As we have seen in section 4, this extra conserved quantity implies that the Maxwell–Schrödinger dynamics decomposes locally into the Cartesian product of a flow on $\mathbb{C}^2$ (in the (x, z) coordinates in (4.2)) times action–angle dynamics for the pair (L, φ). The reduced (x, z) flow on $\mathbb{C}^2$ has a spiral–saddle fixed point (this is the periodic orbit O_ϵ^L in the full phase space $\mathbb{C}^3$); so we seek the analogy of the Devaney construction of the Maxwell–Schrödinger case.

The local map Φ_0 in the first part of Devaney's construction extends easily to the Maxwell–Schrödinger case simply by applying it to the $\mathbb{C}^2$ part of the flow in terms of the reduced coordinates x and z in the vicinity of the perturbed periodic orbit O_ϵ^L. The global part Φ_1 of the return map is obtained in the Maxwell–Schrö dinger case by lifting the dynamics to $\mathbb{C}^3$ (with coordinates (x, u, v)), flowing along the two-dimensional homoclinic intersection surface back into the vicinity of O_ϵ^L, and then factoring out the angle φ to return to the local coordinates x and z in $\mathbb{C}^2$. By extending Devaney's construction to include the global geometry associated with the action–angle pair (L, φ), we show that iterations of the return map $\Phi = \Phi_0 \circ \Phi_1$ in $\mathbb{C}^3$ now produce a Cantor-set structure times an interval (for L) and a circle (for φ). (For convenience we will define our map Φ as the composite $\Phi = \Phi_0 \circ \Phi_1$; that is, we will take the composition in the reverse order from that in ref. [16].)

The two-dimensional homoclinic *intersection surface* defining the map Φ_1 is the analog for the

Maxwell–Schrödinger case of the one-dimensional Hamiltonian spiral–saddle connection *orbit* in Devaney's construction. In fact, there are two such homoclinic intersection surfaces in the present case in $\mathbb{C}^3$, at $\psi_0 = 0$ and $\psi_0 = \pi$, which would correspond to a pair of Hamiltonian spiral–saddle connection orbits in $\mathbb{C}^2$. Because a pair of intersection surfaces arises in this case, the chaotic dynamics manifest themselves slightly more clearly here than in the case treated by Devaney. Namely, phase points switch intermittently from one intersection surface to the other, and this intermittent switching shows extreme sensitivity to initial conditions.

In the remainder of this section, we explicitly construct the Smale horseshoe for the Maxwell–Schrödinger problem. In this construction, we utilize as much as possible the results obtained by Devaney [16]. In order to construct the Smale horseshoe, we perform the following steps. First, we describe the local decomposition of both the phase space and the invariant manifolds in the vicinity of the periodic orbit O_ϵ^L. Next, we define two local cross-sections to the flow near the stable and unstable manifolds of the periodic orbit O_ϵ^L. These cross-sections are then used to define the maps Φ_0 and Φ_1. And finally, we identify the Cantor-set structure invariant under the return map $\Phi = \Phi_0 \circ \Phi_1$ and describe the chaotic dynamics of phase points whose initial conditions lie in that invariant Cantor set.

The previous three sections show that the probe-laser perturbation causes two-dimensional transverse intersections of the stable and unstable manifolds $\mathscr{W}^s(O_\epsilon^L)$ and $\mathscr{W}^u(O_\epsilon^L)$ of the perturbed periodic orbit O_ϵ^L to occur globally in $\mathbb{C}^3$. Of course, this global structure implies transverse intersections of the manifolds $\mathscr{W}^s(O_\epsilon^L)$ and $\mathscr{W}^u(O_\epsilon^L)$ in any local neighborhood of O_ϵ^L as well. Factoring out the angle φ in this neighborhood reduces the intersections of $\mathscr{W}^s(O_\epsilon^L)$ and $\mathscr{W}^u(O_\epsilon^L)$ to one-dimensional, and expresses them in the local $\mathbb{C}^2$ coordinates (x, z) needed to adapt Devaney's construction to the Maxwell–Schrödinger case.

In the local coordinates (x, z), the perturbed periodic orbit O_ϵ^L is the Cartesian product $P_\epsilon^L \times \varphi$ of a fixed point P_ϵ^L, which lies close to the origin of the (x, z) coordinates, with the angle φ. The manifolds $\mathscr{W}^s(O_\epsilon^L)$ and $\mathscr{W}^u(O_\epsilon^L)$ can also be decomposed as Cartesian products $\mathscr{W}^s(O_\epsilon^L) = \mathscr{W}^s(P_\epsilon^L) \times \varphi$ and $\mathscr{W}^u(O_\epsilon^L) = \mathscr{W}^u(P_\epsilon^L) \times \varphi$, where these relationships are valid locally for the parts of the stable and unstable manifolds close to the perturbed periodic orbit O_ϵ^L and the perturbed equilibrium P_ϵ^L, respectively. Moreover, since the stable manifold $\mathscr{W}^s(O_\epsilon^L)$ intersects the unstable manifold $\mathscr{W}^u(O_\epsilon^L)$, both manifolds return to any small neighborhood of O_ϵ^L. The returning pieces of the stable and unstable manifolds of the periodic orbit O_ϵ^L can also be decomposed locally near O_ϵ^L as Cartesian products; we denote this decomposition of the returning pieces by $\mathscr{W}_R^s \times \varphi$ and $\mathscr{W}_R^u \times \varphi$, respectively. It should be clear that the reduced manifolds $\mathscr{W}_R^s$ and $\mathscr{W}^u(P_\epsilon^L)$, and $\mathscr{W}^s(P_\epsilon^L)$ and $\mathscr{W}_R^u$ intersect transversely, because the original stable and unstable manifolds $\mathscr{W}^s(O_\epsilon^L)$ and $\mathscr{W}^u(O_\epsilon^L)$ of the periodic orbit O_ϵ^L do so.

In order to facilitate the construction of the return map Φ, we translate the perturbed fixed point P_ϵ^L to the origin of the coordinates in $\mathbb{C}^2$. Then, the theorem proven in ref. [28], shows that new local symplectic coordinates (x, z) near the perturbed fixed point P_ϵ^L exist in which the (x, z) part of the flow is given by

$$(x(0), z(0)) \mapsto (e^{(A+iB)t}x(0), e^{-(A+iB)t}z(0)).$$

This flow is generated by the Hamiltonian

$$H = \alpha(xz + x^*z^*) + i\beta(xz - x^*z^*) + \mathscr{O}(4),$$

where $\mathscr{O}(4)$ denotes quartic and higher order polynomials. Here α and β denote the real and the imaginary part of the quartet of the eigenvalues $\pm(\alpha \pm i\beta)$ at the equilibrium P_ϵ^L. The quantities A and B are analytic functions of the initial conditions $x_1(0)$, $x_2(0)$, $z_1(0)$ and $z_2(0)$ in the new phase space coordinates, with $A = \alpha$ and $B = \beta$

at the (x, z) origin $(0,0)$, that is, at the equilibrium P_ϵ^L. (This local representation of the flow is the basis for the ensuing construction of the local map Φ_0.) As for the other variables, L is a constant of motion and φ is a quadrature that decouples from the motion in the new local $\mathbb{C}^2$ variables (x, z). In these new local coordinates, $x = 0$ defines the local stable manifold $\mathscr{W}^s(P_\epsilon^L)$ of the fixed point P_ϵ^L, and $z = 0$ defines its local unstable manifold $\mathscr{W}^u(P_\epsilon^L)$.

We are now ready to define two local transverse cross-sections to the reduced (x, z) flow near the stable and the unstable manifolds $\mathscr{W}^s(P_\epsilon^L)$ and $\mathscr{W}^u(P_\epsilon^L)$ of the equilibrium P_ϵ^L. (The unreduced counterparts of these cross-sections may be obtained by taking their Cartesian products with the angle φ.) For small enough positive numbers d_s, d_u, δ_s and δ_u, the two solid tori

$$\Sigma^s = \{(x,z) | \, |x| \le d_s, |z| = \delta_s\},$$

$$\Sigma^u = \{(x,z) | \, |x| = \delta_u, |z| \le d_u\}$$

are transverse to the reduced flow near the perturbed equilibrium P_ϵ^L. Let σ^s and σ^u be the intersections of the transverse tori Σ^s and Σ^u with the stable and the unstable manifolds $\mathscr{W}^s(P_\epsilon^L)$ and $\mathscr{W}^u(P_\epsilon^L)$ of the fixed point P_ϵ^L. So the intersections σ^s and σ^u are the two center circles of the solid tori Σ^s and Σ^u, respectively. Each of the transverse solid tori Σ^s and Σ^u intersects the manifold $\mathscr{M}_\epsilon^{H,L}$ (with H and L having the same value as for the fixed point P_ϵ^L) in an annulus Σ_0^s or Σ_0^u that contains the appropriate circle σ^s or σ^u. That is, the circles σ^s and σ^u are the intersections of the stable and unstable manifolds $\mathscr{W}^s(P_\epsilon^L)$ and $\mathscr{W}^u(P_\epsilon^L)$ of the fixed point P_ϵ^L with the annuli Σ_0^s and Σ_0^u, respectively.

The reduced manifolds $\mathscr{W}^s(P_\epsilon^L)$ and $\mathscr{W}_R^u$ intersect along two orbits spiraling towards the fixed point P_ϵ^L. Likewise, the reduced manifolds $\mathscr{W}_R^s$ and $\mathscr{W}^u(P_\epsilon^L)$ intersect along two orbits spiraling away from the fixed point P_ϵ^L. Let the two intersection orbits of the reduced manifolds $\mathscr{W}^s(P_\epsilon^L)$ and $\mathscr{W}_R^u$ be denoted by γ_1^s and γ_2^s, and let the intersection orbits of the manifolds $\mathscr{W}_R^s$ and $\mathscr{W}^u(P_\epsilon^L)$ be denoted by γ_1^u, and γ_2^s. We choose the labeling in such a way that the orbits γ_i^s and γ_i^u, with the same i, are the reduced representations of the same intersection surface; that is, the cylinders $\gamma_i^s \times \varphi$ and $\gamma_i^u \times \varphi$ lie on the same branch of the intersection $\mathscr{W}^s(O_\epsilon^L) \cap \mathscr{W}^u(O_\epsilon^L)$ near the perturbed hyperbolic periodic orbit O_ϵ^L. The orbits γ_1^s and γ_2^s intersect the circle σ^s (transversely inside $\mathscr{W}^s(P_\epsilon^L)$) in two points q_1^s and q_2^s. Likewise, the orbits γ_1^u and γ_2^s intersect the circle σ^u (transversely inside $\mathscr{W}^u(P_\epsilon^L)$) in two points q_1^u and q_2^u. Let us also denote by τ_1^s and τ_2^s the two curves of intersection of the reduced manifold $\mathscr{W}_R^u$ with the annulus Σ_0^s, and let us denote by τ_1^u and τ_2^u the two curves of intersection of the reduced manifold $\mathscr{W}_R^s$ with the annulus Σ_0^u. We again choose the labeling in such a way that each curve τ_i^s passes through the corresponding point q_i^s with the same i, and that each curve τ_i^u passes through the corresponding point q_i^u with the same i. (See fig. 11.)

The global flow takes the circle $q_1^u \times \varphi$ into the circle $q_1^s \times \varphi$, and takes the circle $q_2^u \times \varphi$ into the

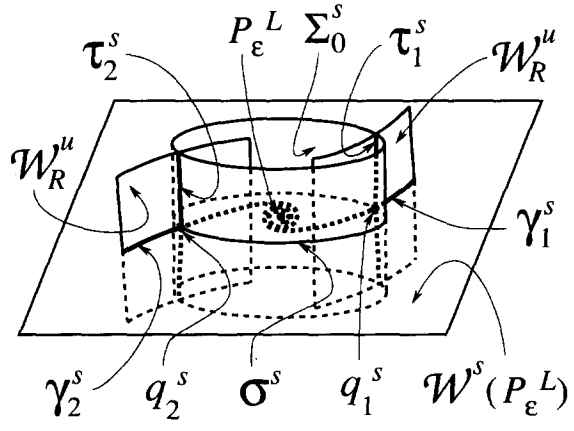

Fig. 11. The reduced manifolds $\mathscr{W}^s(P_\epsilon^L)$ and $\mathscr{W}_R^u$ intersect along two orbits, γ_1^s and γ_2^s, spiraling towards the fixed point P_ϵ^L. The orbits γ_1^s and γ_2^s intersect the circle σ^s in two points q_1^s and q_2^s. The reduced manifold $\mathscr{W}_R^u$ intersects the annulus Σ_0^s along two curves τ_1^s and τ_2^s.

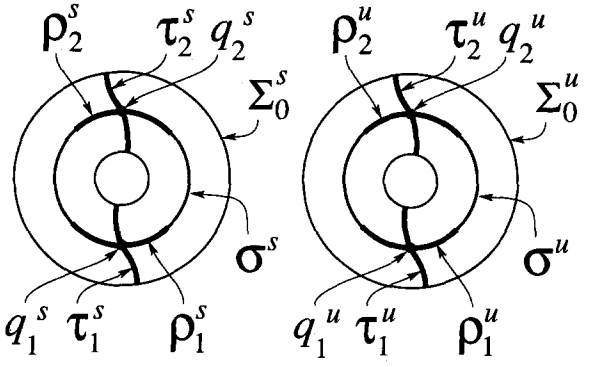

Fig. 12. After factoring out the angle φ, the action of the global flow is to take the points q_1^u and q_2^u into the points q_1^s and q_2^s, respectively. Also, the segments τ_1^u and τ_2^u are taken into the segments ρ_1^s and ρ_2^s, respectively. Likewise, the preimage of the segments τ_1^s and τ_2^s are the segments ρ_1^u and ρ_2^u, respectively.

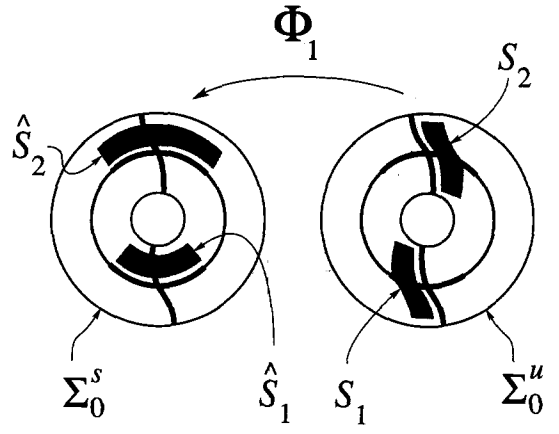

Fig. 13. The first step in the construction of the Smale horseshoe is the map Φ_1, which takes two strips S_1 and S_2 on Σ_0^u into two strips $\hat{S}_1$ and $\hat{S}_2$ on Σ_0^s.

circle $q_2^s \times \varphi$. It also takes the cylinder $\tau_1^u \times \varphi$ into a cylindrical piece $\rho_1^s \times \varphi$ of the torus $\sigma^s \times \varphi$ around the circle $q_1^s \times \varphi$, and takes the cylinder $\tau_2^u \times \varphi$ into a cylindrical piece $\rho_2^s \times \varphi$ of the torus $\sigma^s \times \varphi$ around the circle $q_2^s \times \varphi$. Likewise, the preimage of the cylinder $\tau_1^s \times \varphi$ is a cylindrical piece $\rho_1^u \times \varphi$ of the torus $\sigma^u \times \varphi$ around the circle $q_1^u \times \varphi$, and the preimage of the cylinder $\tau_2^s \times \varphi$ is a cylindrical piece $\rho_2^u \times \varphi$ of the torus $\sigma^u \times \varphi$ around the circle $q_2^u \times \varphi$. (See fig. 12.)

We may now construct the Smale horseshoe for our return map Φ. We first choose two strips S_1 and S_2 in the annulus Σ_0^u close to and parallel to the curves τ_1^u and τ_2^u, respectively. We then map the solids of revolution $S_1 \times \varphi$ and $S_2 \times \varphi$ into the transverse section $\Sigma_0^s \times \varphi$ by using the global flow. This mapping constitutes the global part, Φ_1, of the return map Φ. The resulting images are two solids of revolution $\hat{S}_1 \times \varphi$ and $\hat{S}_2 \times \varphi$, where $\hat{S}_1$ and $\hat{S}_2$ are two strips in the annulus Σ_0^s parallel to, and close to the curves ρ_1^s and ρ_2^s, respectively. (See fig. 13.) Then, we use the local (x, z) representation of the flow (8.1) to show (just as in ref. [16], lemma, p. 434) that the images of the strips S_1 and S_2 are two pieces of fat spirals, V_1 and V_2, lying in the annulus Σ_0^u and wrapping towards the circle σ^u. (See fig. 14.) By adjusting the thickness of the strips S_1 and S_2, we can arrange for the pieces of spirals, V_1 and V_2, to intersect S_1 and S_2 each in one connected piece. (See fig. 15.) The mapping of $\hat{S}_1 \times \varphi$ and $\hat{S}_2 \times \varphi$ into $V_1 \times \varphi$ and $V_2 \times \varphi$, respectively, constitutes the local part, Φ_0, of the return map Φ. The complete return map, Φ, is the composition $\Phi = \Phi_0 \circ \Phi_1$.

After factoring out the angle φ, the return map Φ constructed in this way takes the two strips S_1 and S_2, lying in the annulus Σ_0^u in (x, z) coordinates, into two pieces of fat spirals, V_1 and V_2, lying in the same annulus. This factored map is

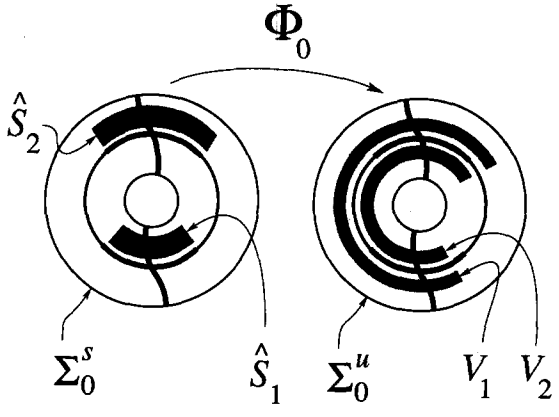

Fig. 14. The second step in the construction of the Smale horseshoe is the map Φ_0, which stretches the strips $\hat{S}_1$ and $\hat{S}_2$ on Σ_0^s radially, compresses them azimuthally, and takes them into two pieces of "fat spirals" V_1 and V_2 on Σ_0^u.

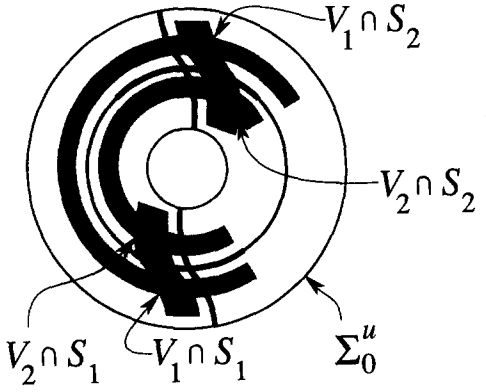

Fig. 15. On Σ_0^u, the combined map $\Phi_0 \circ \Phi_1$ stretches the two strips S_1 and S_2 azimuthally, compresses them radially, and reinjects them over their original region as two pieces of "fat spirals" V_1 and V_2. Thus, $\Phi_0 \circ \Phi_1$ is a Smale horseshoe map.

the Smale horseshoe map for our problem. In a similar fashion as in ref. [16], one may also show that the proper stretching and contraction conditions are satisfied for this map. Therefore, an invariant Cantor set, Λ, of points exists inside the rectangles $S_1 \cap V_1$, $S_1 \cap V_2$, $S_2 \cap V_1$ and $S_2 \cap V_2$, on which the return map acts as a shift on two symbols. To each point in the Cantor set Λ we can associate a bi-infinite sequence of the digits 1 and 2, where the nth digit tells whether the point is in the strip S_1 or the strip S_2.

In terms of the original dynamics, the bi-infinite sequences denote circles $p \times \varphi$ where p is a point in the invariant Cantor set Λ. Each point starting on one of these circles will be contained in one of the sets $S_i \times \varphi$ $(i = 1, 2)$ after the nth iterate of the return map, and will therefore follow one of the orbits in the ith intersection surface $(i = 1, 2)$, while flowing away from the perturbed periodic orbit O_ϵ^L and then back to it. The correspondence between the circles in the invariant Cantor set of circles $\Lambda \times \varphi$ and the set of bi-infinite sequences of the digits 1 and 2 is one-to-one. Hence, for any given bi-infinite sequence of 1's and 2's, there exists a circle of initial conditions in the invariant Cantor set $\Lambda \times \varphi$ whose orbit switches back and forth in the two intersection surfaces exactly as in the given sequence. Together with the extreme sensitivity to initial conditions near the Cantor set $\Lambda \times \varphi$, these switching sequences constitute the mechanism for chaotic behavior in our system.

9. Physical consequences

In conclusion, we discuss the physical consequences of the chaotic dynamics implied by the transverse homoclinic intersections found in this paper. First, we describe the behavior of a typical chaotic trajectory determined from the chaotic dynamics obtained in the preceding sections. We then make a few observations concerning measurability of the effects we predict using our Maxwell–Schrödinger model.

In the previous section, we have characterized the chaotic dynamics found in the Maxwell–Schrödinger model as chaotic switching of trajectories (with initial conditions in the invariant Cantor set) between two homoclinic intersection surfaces. This means that in the $(\mathscr{E}, b_+, b_-)$ envelope coordinates, the time series for a chaotic trajectory could be well approximated by inserting *random* parameters into the expressions for the homoclinic solutions according to

$$\mathscr{E} = \pm\sqrt{2L}\,\operatorname{sech}\left[\sqrt{2L}\,(t - t_\mu)\right],$$

$$b_+ = \pm i\sqrt{2L}\,\tanh\left[\sqrt{2L}\,(t - t_\mu)\right] e^{i\theta_\mu},$$

$$b_- = \pm\sqrt{2L}\,\operatorname{sech}\left[\sqrt{2L}\,(t - t_\mu)\right] e^{i\theta_\mu},$$

over time intervals $\tau_{\mu-1} < t < \tau_\mu$. Here, the parameters t_μ, θ_μ and τ_μ and the sign may be chosen from a random process, μ varies over the integers, and $\tau_{\mu-1} < t_\mu < \tau_\mu$ for all μ. The phases $\theta_{\mu-1}$ and θ_μ must also be $\mathscr{O}(\epsilon)$ or $\mathscr{O}(\omega)$ close to each other, depending on whether ϵ or ω is the small parameter. By continuity, any trajectory close to a chaotic trajectory may also be well approximated by the same type of expressions for a finite amount of time.

A typical wave form of the time series for the electric field envelope $\mathscr{E}$ (that is, the brightness

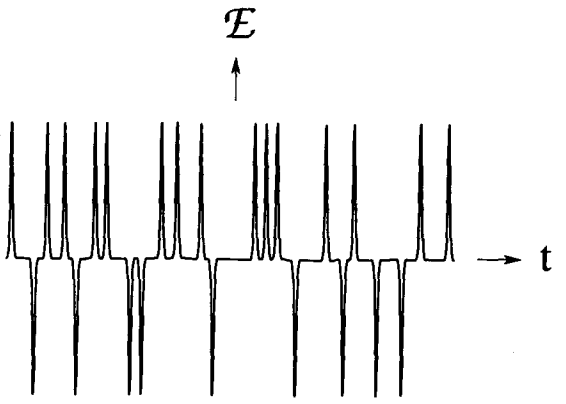

Fig. 16. The time series for the perturbed electric field envelope, $\mathcal{E}$, shows randomly switching sech-like profiles.

of the light emitted by our laser–matter system) for a typical chaotic trajectory is sketched in fig. 16. This figure shows that the intensity $|\mathcal{E}|^2$ of the emitted light will "flicker" in a chaotic fashion on $\mathcal{O}(1)$ time scales[#4]. By the above discussion, we see that this chaotic flickering will occur at least for a finite amount of time for material samples which are initially close to having all the atoms in the excited state.

Dynamical systems methods thus predict chaotic flickering in the output intensity of a unidirectional lasing medium (or a superflourescent medium, see refs. [29, 30] in a single-mode, lossless, ring cavity, due to perturbation by a phase-matched probe laser. This prediction applies in the good-cavity limit, and, thus, during the time before losses can cause decay into steady states, such as the steady phase-locked states discussed in ref. [31]. Because all real experiments possess some losses, the Hamiltonian model discussed here may be expected to predict only a transient effect. Strictly speaking, any modification of the Hamiltonian model discussed here that would include dissipation would probably destroy the homoclinic chaos, because losses would destroy conservation of the Hamiltonian, H, and unitarity, L, upon whose constant level surfaces the transverse intersections found here take place. Therefore, it might not be possible to construct the Smale horseshoe. Nonetheless, the dynamics in the dissipative model would be similar to the dynamics in our Hamiltonian model at least on finite time intervals, and the smaller the dissipation, the longer these time intervals.

In practice, nearly lossless gain–feedback experiments are presently being carried out in the study of transient optical instabilities in high-Q ring cavities [32]. In these experiments, lasing by Raman processes is seen to occur in only one direction, namely in the direction of the probe. Such experiments approximate some of the conditions under which the present model is derived (lossless, unidirectional, single-polarization lasing with phase-matched probe) and provide an indication that new experiments may be designed to approximate the conditions stated in this paper more closely. We believe that measuring the chaotic flickering due to the effect of a probe laser on the output of a unidirectional lasing medium is a fruitful direction for further experimental investigation of transient effects in the dynamics of high-Q ring-cavity lasers.

A link between the chaotically flickering signal predicted in this paper and the signal produced in an experiment may be established by using various diagnostic procedures. The simplest such procedure is the comparison of the power spectra of the theoretically predicted solutions with the experimental output. The form of the power spectrum of the light intensity $\mathcal{E}$ produced by the chaotic trajectories in our Maxwell–Schrödinger model may be computed by the methods of Brundsen and Homes [33] and Brundsen, Cortell, and Holmes [34]. In a properly prepared experiment, that is, one in which $\kappa \ll \epsilon \ll 1$ or $\kappa \ll \omega \ll 1$, the homoclinic chaos predicted in this paper should dominate over the chaos produced by the breakup of subharmonic resonance bands and their subsequent interaction. Thus, in such an experiment, material samples whose atoms are

[#4]Recall from section 2 that since $\kappa \ll 1$, it makes sense to discuss the brightness of light (but not its frequency, that is, color) on the $\mathcal{O}(1)$ time scales of the slowly varying envelope approximation. Also, recall that $\mathcal{O}(1)$ time in our nondimensional variables is $\mathcal{O}(1/\omega_c)$ time in seconds.

initially all close to the excited state should produce signals whose power spectra would compare favorably with those calculated by using the Maxwell–Schrödinger model. Samples that are initially less excited should, in turn, produce power spectra that are almost discrete, and only slightly broadened due to the weak effects of the subharmonic chaos.

The power spectrum of the emitted light intensity is just one of the easily measurable quantities which may be calculated by using the Maxwell–Schrödinger model. Finding and calculating other such quantities and comparing them with experimental results present interesting theoretical and experiment and would cast additional light on the field of chaotic laser–matter dynamics.

Acknowledgements

The authors are grateful to A. Aceves, A. Calini, R. Camassa, D. David, R. Easton, J. Elgin, I. Gabitov, J.D. Gibbon, M. Herrera, P. Holmes, J. Moloney, W. Newman, J. Palimore, A. Rouhi, B. Sundaram and E. Wright for helpful comments and encouragement during the course of this work.

Appendix A. Restricted perturbed Maxwell–Bloch dynamics

In this appendix we analyze the homoclinic chaos found in a simplified three-dimensional Maxwell–Bloch model of laser–matter dynamics. As we shall see, this simplified model is essentially the same as the approximate pendulum model discussed in ref. [11]. The simplified three-dimensional Maxwell–Bloch model also possesses global geometric structures analogous to those used in the main body of the paper.

Starting from the perturbed Maxwell–Schrödinger equations (2.1), the perturbed Maxwell–Bloch equations are derived by rescaling $\tilde{\mathscr{E}} = 2\mathscr{E}$, $\tilde{\epsilon} = 2\epsilon$, and introducing the following phase-invariant variables (Stokes parameters):

$$\mathscr{P} = 2ib_+ b_-^*, \quad \mathscr{D} = |b_+|^2 - |b_-|^2,$$

where (dropping the tilde) $\mathscr{E} = \mathscr{E}_1 + i\mathscr{E}_2$ and $\mathscr{P} = \mathscr{P}_1 + i\mathscr{P}_2$ are complex and $\mathscr{D}$ is real. The resulting perturbed Maxwell–Bloch equations are

$$\dot{\mathscr{E}} = \mathscr{P}, \tag{A.1a}$$

$$\dot{\mathscr{P}} = (\mathscr{E} + \epsilon e^{i\omega t})\mathscr{D}, \tag{A.1b}$$

$$\dot{\mathscr{D}} = -\tfrac{1}{2}\left[(\mathscr{E} + \epsilon e^{i\omega t})\mathscr{P}^* + (\mathscr{E}^* + \epsilon e^{-i\omega t})\mathscr{P}\right]. \tag{A.1c}$$

The perturbed Maxwell–Bloch problem inherits the homoclinic structure and the chaotic dynamics discussed in the text for the perturbed Maxwell–Schrödinger equations, simply as a result of this change to phase-invariant variables. In the Maxwell–Bloch representation of this problem, the transverse intersection surfaces discussed in the text become true Hamiltonian spiral–saddle connection orbits in a rotating frame. (See ref. [35].) In the fixed frame, these chaotic dynamics in the vicinity of the Hamiltonian spiral–saddle connection orbits remain near the two unperturbed homoclinic orbits given by

$$\mathscr{E} = \pm\sqrt{K}\,\mathrm{sech}(\sqrt{K}\,t),$$

$$\mathscr{P} = \mp\sqrt{K}\,\mathrm{sech}(\sqrt{K}\,t)\tanh(\sqrt{K}\,t),$$

$$\mathscr{D} = K\left[1 - 2\,\mathrm{sech}^2(\sqrt{K}\,t)\right],$$

which lie in the real subspace $\mathscr{E}_2 = 0 = \mathscr{P}_2$. (Here, K is a constant parameter.) Thus, the chaotic motion resulting from the perturbation stays near the real subspace.

This situation suggests modeling the chaotic dynamics by taking the real parts of all quantities, including the perturbation terms, in the perturbed Maxwell–Bloch equations. The resulting approximate dynamics for the perturbed problem

are governed by the following equations:

$$\dot{\mathscr{E}} = \mathscr{P}, \tag{A.2a}$$

$$\dot{\mathscr{P}} = [\mathscr{E} + \epsilon \cos(\omega t)]\mathscr{D}, \tag{A.2b}$$

$$\dot{\mathscr{D}} = -[\mathscr{E} + \epsilon \cos(\omega t)]\mathscr{P}, \tag{A.2c}$$

where from now on all quantities are taken to be *real*.

This system is Hamiltonian with a noncanonical Lie–Poisson bracket

$$\{\mathscr{E}, \mathscr{P}\} = -\mathscr{D}, \quad \{\mathscr{E}, \mathscr{D}\} = \mathscr{P}, \quad \{\mathscr{P}, \mathscr{D}\} = 0,$$

and time-dependent Hamiltonian $\mathscr{H} = \frac{1}{2}[\mathscr{E} + \epsilon \cos(\omega t)]^2 + \mathscr{D}$. (For a discussion of Lie–Poisson brackets, see appendix B.) System (A.2) possesses the constant of motion $L = \frac{1}{2}\mathscr{P}^2 + \frac{1}{2}\mathscr{D}^2$, which is the same as the unitarity constant L in the text, and is the Casimir function for the Lie–Poisson bracket. For $\epsilon = 0$, the Hamiltonian $\mathscr{H}$ reduces to another conserved quantity $K = \frac{1}{2}\mathscr{E}^2 + \mathscr{D}$, the sum of the atomic and the field energies in the system. Linearity of this conserved quantity allows $\mathscr{D}$ to be eliminated in favor of K.

The system (A.2) is the new $(\mathscr{E}, \mathscr{P}, K)$ variables, namely,

$$\dot{\mathscr{E}} = \mathscr{P}, \tag{A.3a}$$

$$\dot{\mathscr{P}} = [\mathscr{E} + \epsilon \cos(\omega t)]\left(K - \tfrac{1}{2}\mathscr{E}^2\right), \tag{A.3b}$$

$$\dot{K} = -\epsilon \mathscr{P} \cos(\omega t), \tag{A.3c}$$

thus becomes a perturbed Duffing oscillator, with a slowly varying parameter, K. The constant of motion L for this oscillator system is given by

$$L = \tfrac{1}{2}\mathscr{P}^2 + \tfrac{1}{2}\left(K - \tfrac{1}{2}\mathscr{E}^2\right)^2.$$

The motion takes place on the surfaces of constant L. For $\epsilon = 0$, the system (A.3) reduces to a parametrized family of Duffing oscillators,

$$\dot{\mathscr{E}} = \mathscr{P}, \quad \dot{\mathscr{P}} = \mathscr{E}\left(K - \tfrac{1}{2}\mathscr{E}^2\right).$$

In the $(\mathscr{E}, \mathscr{P}, K)$ space, its orbits are the intersections of the surfaces $\mathscr{M}^L = \{(\mathscr{E}, \mathscr{P}, K) | L(\mathscr{E}, \mathscr{P}, K) = \text{constant}\}$ with the horizontal planes $K = \text{constant}$. Orbits on a surface $\mathscr{M}^L$ are shown in fig. 17.

A homoclinic manifold exists for positive K, given by the equation

$$L - \tfrac{1}{2}K^2 = 0, \tag{A.4}$$

or, explicitly in the $(\mathscr{E}, \mathscr{P}, K)$ coordinates,

$$\mathscr{P}^2 - K\mathscr{E}^2 + \tfrac{1}{4}\mathscr{E}^4 = 0.$$

Motion takes place along the homoclinic orbits, described implicitly by eqs. (A.4) and $K = \text{constant}$, or parametrized by the solutions

$$\mathscr{E} = \pm\sqrt{K}\,\operatorname{sech}(\sqrt{K}\,t),$$

$$\mathscr{P} = \mp\sqrt{K}\,\operatorname{sech}(\sqrt{K}\,t)\tanh(\sqrt{K}\,t).$$

These orbits lie on the intersections of three surfaces, a surface $\mathscr{M}^L$, a plane $K = \text{constant}$, and the homoclinic manifold $L - \frac{1}{2}K^2 = 0$. (See fig. 18.)

For nonzero ϵ, the three-dimensional perturbed Maxwell–Bloch equations cannot be made autonomous by a phase rotation, in contrast to their five- and six-dimensional counterparts.

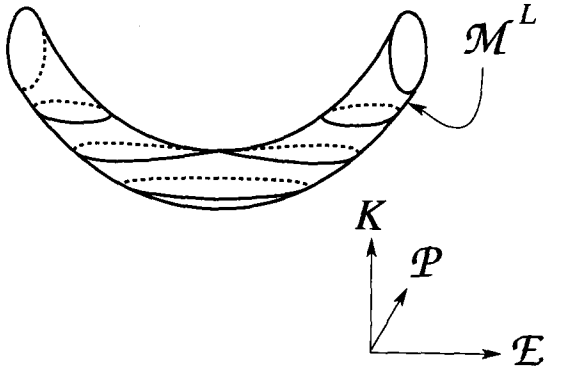

Fig. 17. Unperturbed periodic and homoclinic orbits lie on the energy surface $\mathscr{M}^L$ in $\mathbb{R}^3$ for the restricted Maxwell–Bloch dynamics.

Therefore, a slightly different mechanism is responsible for the existence of chaotic dynamics. This mechanism for chaos turns out to be the usual homoclinic tangle, appearing in the Poincaré map $t \mapsto t + 2\pi/\omega$.

In fact, restricting to a level surface of L by setting

$$\mathscr{P} = \sqrt{2L}\cos\phi, \quad \mathscr{Q} = \sqrt{2L}\sin\phi,$$

in eqs. (A.3) gives the periodically perturbed pendulum equations

$$\dot{\mathscr{E}} = \sqrt{2L}\cos\phi, \quad \dot{\phi} = -[\mathscr{E} + \epsilon\cos(\omega t)],$$

parametrized by the value of L. This perturbed pendulum system is essentially the same as the approximate model discussed in Alekseev and Berman [11]. The Poincaré-section analysis of this problem is very similar to the standard textbook example of the Smale horseshoe construction. (See, e.g., ref. [36].) This representation of the restricted perturbed Maxwell–Bloch problem as a parametrized family of perturbed pendula provides the setting for the simplest analysis of chaotic dynamics available for this problem. However, to demonstrate in a bare-hands example the type of global phase-space geometry we use in the text, and to visualize this type of geometry in a realistic way, we will return to the Duffing oscillator representation of this problem.

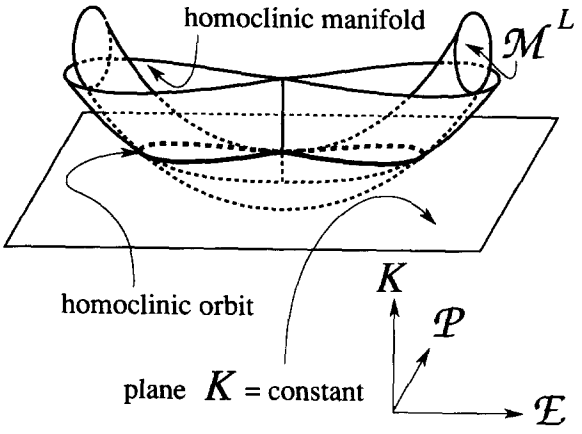

Fig. 18. A homoclinic orbit is the intersection of three surfaces in $\mathbb{R}^3$, a surface $\mathcal{M}^L$, a plane K = constant, and the homoclinic manifold $L - \frac{1}{2}K^2 = 0$.

Before returning to the Duffing oscillator representation, however, we will take advantage of the parametrized pendulum representation in order to show persistence of the hyperbolic structures in this problem without resorting to the general abstract theory. Namely, the hyperbolic fixed point of the pendulum at $\phi = \pm\pi$ persists under the perturbation for $\epsilon \ll 1$ as a hyperbolic periodic orbit in the extended $(\mathscr{E}, \phi, t)$ phase space. Morever, the stable and unstable manifolds of the fixed point survive as the stable and unstable manifolds of this periodic orbit. These results appear in the extended $(\mathscr{E}, \phi, K, t)$ phase space of the Duffing oscillator in the following way. First, the line of hyperbolic fixed points parametrized by K survives under the perturbation as a cylinder of hyperbolic periodic orbits in the $(\mathscr{E}, \mathscr{P}, K, t)$ phase space. The stable and unstable manifolds of the hyperbolic fixed points persist as the stable and unstable manifolds of these periodic orbits.

We now construct a three-dimensional Poincaré slice by fixing $t = 0$, and taking periodicity of the problem into account. In this Poincaré slice, the perturbed cylinder of hyperbolic periodic orbits appears as a curve of equilibria in $(\mathscr{E}, \mathscr{P}, K)$ space. The perturbed stable and unstable manifolds of the equilibria on this curve each lie close to the unperturbed homoclinic orbits. The union of these manifolds are two smooth surfaces lying close to the unperturbed homoclinic manifold. (This situation is similar to the one shown in fig. 7.) We will show shortly that these stable and unstable manifolds of the perturbed equilibria intersect transversely in the Poincaré slice. Both the stable and the unstable manifolds of a given perturbed equilibrium and their intersections lie on one of the surfaces $\mathcal{M}^L$ and produce the usual homoclinic tangle. By the Poincaré–Birkhoff–Smale homoclinic theorem [27, 36], this tangling results in a Smale horseshoe construction for a certain sufficiently large iterate of the Poincaré

map, and this implies the existence of chaotic dynamics.

We calculate the distance between the stable and the unstable manifolds of an equilibrium lying on the curve of equilibria for the Poincaré map by calculating the Melnikov function along one of the normals to an unperturbed homoclinic orbit. We parametrize the perturbed stable and unstable manifolds of the fixed points in the Poincaré section by the unperturbed homoclinic solution taken at time $-t_0$. Namely,

$$\mathscr{E} = \pm\sqrt{K}\,\operatorname{sech}\left[\sqrt{K}(-t_0)\right],$$

$$\mathscr{P} = \mp\sqrt{K}\,\operatorname{sech}\left[\sqrt{K}(-t_0)\right]\tanh\left[\sqrt{K}(-t_0)\right],$$

K = constant,

$t = 0$.

As t_0 varies, this solution traces out the homoclinic orbit lying on a level surface of L, $\mathscr{M}^L$. The two normal vectors to the homoclinic orbit at the given point a in $(\mathscr{E}, \mathscr{P}, K)$ space are given by taking the gradients of the two relations $K =$ constant and $L - \frac{1}{2}K^2 = 0$. Namely, in $(\mathscr{E}, \mathscr{P}, K)$ coordinates,

$$\boldsymbol{n}_1 = \nabla K = (0,0,1),$$

$$\boldsymbol{n}_2 = \nabla\left(L - \tfrac{1}{2}K^2\right) = \left(-\mathscr{E}\left[K - \tfrac{1}{2}\mathscr{E}^2\right], \mathscr{P}, -\tfrac{1}{2}\mathscr{E}^2\right).$$

These two normals span the plane normal to the unperturbed homoclinic orbit in the $(\mathscr{E}, \mathscr{P}, K)$ space at the point a. The perturbed stable and unstable manifolds intersect this plane at the points a_ϵ^s and a_ϵ^u as discussed in the text. The vector $a_\epsilon^u - a_\epsilon^s$ has two components in this plane. However, since both points lie on the same level surface of L, $\mathscr{M}^L$, it is clear that we need to compute the vanishing of only one component of this vector, in order to show intersection of the stable and unstable manifolds of the perturbed fixed point in the Poincaré section at $t = 0$. (Compare with fig. 9.)

The value of the perturbation at the point a is given by

$$\boldsymbol{g} = \big(0, \left[K - \tfrac{1}{2}\mathscr{E}^2(-t_0)\right]\cos(\omega t), -\mathscr{P}(-t_0)\sin(\omega t)\big)\big|_{t=0},$$

since the point a is taken in the $t = 0$ Poincaré slice. In the computation of the Melnikov function we choose the normal component $\boldsymbol{n}_2$. The Melnikov function is computed along the unperturbed trajectory starting at the point a at time $t = 0$. Hence,

$$M(t_0; K; \omega) = \int_{-\infty}^{\infty} \left\langle \boldsymbol{n}_2(a(t - t_0)), \boldsymbol{g}(a(t - t_0), t)\right\rangle \mathrm{d}t$$

$$= \pi\sqrt{K}\,\operatorname{sech}\left(\frac{\pi\omega}{2\sqrt{K}}\right)\sin(\omega t_0),$$

which has simple zeros at $t_0 = n\pi/\omega$. Since these zeros are simple, the stable and unstable manifolds of the perturbed fixed point for the Poincaré map intersect transversely on the level surface $\mathscr{M}^L$ in the Poincaré section at $t = 0$, as shown in fig. 19. (The proof of transversality is the same as in the text; see also fig. 10.) Having found transverse intersections of these manifolds in the Poincaré slice, one may now invoke the Poincaré–Birkhoff–Smale theorem to conclude there exists an iterate of the Poincaré map for

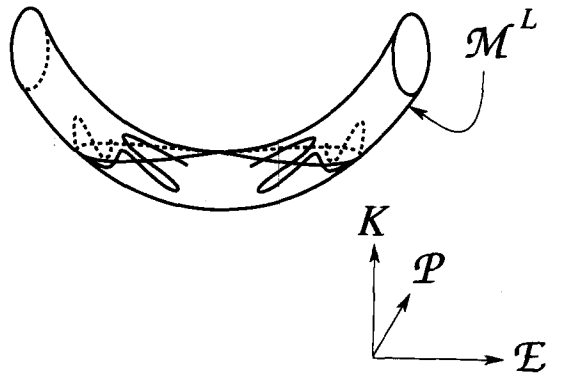

Fig. 19. The stable and unstable manifolds of a perturbed fixed point of the Poincaré map intersect transversely on a surface $\mathscr{M}^L$ in the Poincaré section at $t = 0$.

which the dynamics are equivalent to a Bernoulli shift on two symbols. Physically, as discussed in the text, this type of homoclinic chaos corresponds to random "flickering" of the light intensity emitted by the perturbed system.

Appendix B. Poisson brackets and symplectic forms for Maxwell–Schrödinger and Maxwell–Bloch dynamics

In the body of this paper, several canonical transformations and coordinate changes appear which utilize the underlying Hamiltonian structures of the Maxwell–Schrödinger and Maxwell–Bloch equations. In this appendix we collect the facts about Hamiltonian systems that are needed explicitly in the analysis presented in the text. For comprehensive treatments, see refs. [37–39].

An even-dimensional manifold $\mathcal{M}$ is said to be a *symplectic manifold if* it possesses a non-degenerate, closed 2-form Ω given locally by

$$\Omega = \tfrac{1}{2}K_{ab}(x)\,\mathrm{d}x^a \wedge \mathrm{d}x^b,$$

with $\det K \neq 0$ everywhere, and $a, b = 1,\ldots,2n$. Corresponding to each closed 1-form, expressible locally as $(\partial H/\partial x^b)\,\mathrm{d}x^b$ on a symplectic manifold $\mathcal{M}$, the 2-form Ω determines a local Hamiltonian system according to

$$\dot{x}^a = J^{ab}(x)\,\frac{\partial H}{\partial x^b},$$

where $J = K^{-1}$ is called the Hamiltonian matrix. The Hamiltonian matrix $J^{ab} = \{x^a, x^b\}$ is the matrix of *Poisson brackets* among the coordinates for $\mathcal{M}$. Indeed, the operation defined by

$$\{F,H\} = \frac{\partial F}{\partial x^a}J^{ab}\frac{\partial H}{\partial x^b} = \langle \nabla F, J\,\nabla H\rangle,$$

between pairs of functions F and H on a symplectic manifold, is a bilinear, skew-symmetric map $F\times H \to \{F,H\}$ which satisfies the Jacobi identity,

$$\{F,\{G,H\}\} + \{G,\{H,F\}\} + \{H,\{F,G\}\} = 0,$$

by virtue of the closure of Ω, namely $\mathrm{d}\Omega = 0$. Hence, the operation $\{F,H\}$ defined in this way determines a Poisson bracket.

Two most common examples are the following:

(a) The *canonical* 2-form $\Omega = \mathrm{d}p \wedge \mathrm{d}q$ on $\mathbb{R}^2$ is closed because it is exact, $\Omega = \mathrm{d}(p\,\mathrm{d}q)$. If we set $x = (q,p)$, then it follows that

$$K = \begin{pmatrix} 0 & -1 \\ 1 & 0 \end{pmatrix}, \quad J = \begin{pmatrix} 0 & 1 \\ -1 & 0 \end{pmatrix}, \quad \{q,p\} = 1,$$

and the associated Hamiltonian system is the canonical one,

$$\dot{q} = \frac{\partial H}{\partial p}, \quad \dot{p} = -\frac{\partial H}{\partial q}.$$

(b) The complex symplectic form $\Omega = (1/2\mathrm{i})\,\mathrm{d}z \wedge \mathrm{d}z^*$ on $\mathbb{C}$ follows from the canonical 2-form by setting $z = p + \mathrm{i}q$, $z^* = p - \mathrm{i}q$. The complex canonical Poisson bracket is $\{z, z^*\} = -2\mathrm{i}$.

Both examples (a) and (b) appear in the treatment of the Maxwell–Schrödinger equations in the text.

Transformations leaving Ω invariant are called *canonical*. (In particular, the transformation generated by the phase flow of any Hamiltonian system is canonical, see ref. [38].) The variable transformations for the Maxwell–Schrödinger equations in the text are shown in each case to be canonical, by explicitly giving the 2-form Ω resulting in the new coordinates.

The text and appendix also introduce non-canonical Poisson brackets. For example, the passage from the Maxwell–Schrödinger equations to the complex Maxwell–Bloch equations introduces the following bilinear coordinate transformation to phase-invariant matter variables (Stokes variables):

$$\mathscr{P} = 2\mathrm{i}b_+b_-^*, \quad \mathscr{D} = |b_+|^2 - |b_-|^2.$$

Direct computation using the complex symplectic Poisson brackets $\{b_+, b_+^*\} = -2\mathrm{i} = \{b_-, b_-^*\}$ for b_+ and b_- gives the Poisson brackets

$$\{\mathscr{P}_1, \mathscr{P}_2\} = 4\mathscr{D}, \quad \{\mathscr{P}_2, \mathscr{D}\} = 4\mathscr{P}_1,$$
$$\{\mathscr{D}, \mathscr{P}_1\} = 4\mathscr{P}_2,$$

where $\mathscr{P} = \mathscr{P}_1 + \mathrm{i}\mathscr{P}_2$. Choosing coordinates $\boldsymbol{x} = (x_1, x_2, x_3) = (\mathscr{P}_1/4, \mathscr{P}_2/4, \mathscr{D}/4)$ with Poisson brackets $\{x_i, x_j\} = \epsilon_{ijk} x_k$ allows us to introduce a 2-form Ω as

$$\Omega = \tfrac{1}{3}(x_1\, \mathrm{d}x_2 \wedge \mathrm{d}x_3 + x_2\, \mathrm{d}x_3 \wedge \mathrm{d}x_1 + x_3\, \mathrm{d}x_1 \wedge \mathrm{d}x_2) = \tfrac{1}{6}\epsilon_{ijk} x_k\, \mathrm{d}x_i \wedge \mathrm{d}x_j.$$

This 2-form is neither closed (since $\mathrm{d}\Omega = \mathrm{d}x_1 \wedge \mathrm{d}x_2 \wedge \mathrm{d}x_3$) nor nondegenerate (since, for $M = \frac{1}{2}(x_1^2 + x_2^2 + x_3^2)$, the vector ∇M annihilates the 2-form Ω under substitution). Moreover, the manifold $\mathscr{M} = \mathbb{R}^3$ with coordinates (x_1, x_2, x_3) is not even-dimensional. However, the Poisson bracket associated with this 2-form defined as

$$\{F, H\}\, \mathrm{d}\Omega = \mathrm{d}M \wedge \mathrm{d}F \wedge \mathrm{d}H = \nabla M \cdot \nabla F \times \nabla G\, \mathrm{d}\Omega$$

does satisfy the Jacobi identity for any smooth function M. When restricted to a level surface of M, this Poisson bracket becomes symplectic with Ω given by the area element on that surface. The equations of motion on $\mathbb{R}^3$ associated with this bracket are in cross-product form

$$\dot{\boldsymbol{x}} = \nabla M \times \nabla H,$$

so the motion in $\mathbb{R}^3$ takes place along intersections of level surfaces of M and H. When M is quadratic as in the present case, this Poisson bracket is an example of a Lie–Poisson bracket. (See, e.g., ref. [38], appendix 14, and references therein for general discussions of Lie–Poisson brackets.) The complete Poisson bracket for the complex Maxwell–Bloch dynamics consists of the Lie–Poisson bracket in $\mathbb{R}^3$ for the matter variables $\mathscr{P}$ and $\mathscr{D}$ in direct sum with the complex symplectic bracket for the electric field envelope.

The real restriction of the perturbed Maxwell–Bloch equations in appendix A, system (A.2), may also be written in the cross-product form, by setting $\boldsymbol{x} = (\mathscr{E}, \mathscr{P}, \mathscr{D})$, $M = \frac{1}{2}(x_2^2 + x_3^2) = L$, and $H = \frac{1}{2}[x_1 + \epsilon\cos(\omega t)]^2 + x_3$.

Appendix C. Variational principles for Maxwell–Schrödinger equation sets

This appendix presents the variational principles for the primitive Maxwell–Schrödinger equations and our approximate envelope Maxwell–Schrödinger equations. In particular, starting with the variational principle for the primitive Maxwell–Schrödinger equations, we introduce envelope coordinates and an external perturbing field (the probe laser) to derive the perturbed Maxwell–Schrödinger envelope equations (2.1) treated in the text. This derivation complements the derivation presented in section 2, based solely on the equations of motion, and explains the Hamiltonian nature of the approximate equations and their constants of motion. The primitive Maxwell–Schrödinger equations are

$$E_{zz} - E_{tt} = 2\kappa P_{tt}, \tag{C.1a}$$

$$\mathrm{i}\dot{a}_+ = \frac{1}{2\kappa} a_+ - E a_-, \tag{C.1b}$$

$$\mathrm{i}\dot{a}_- = -\frac{1}{2\kappa} a_- - E a_+, \tag{C.1c}$$

where $P = (a_+ a_-^* + a_+^* a_-)$ is the dimensionless polarizability and the ratio of frequencies, $\kappa = \omega_c/\omega_0 \ll 1$, is a small parameter. The wave equation for the linearly polarized electric field E follows from Maxwell's equations

$$\dot{D} = B_z, \tag{C.2a}$$

$$\dot{B} = E_z, \tag{C.2b}$$

where $D = E + 2\kappa P$ is the electric displacement and B is the magnetic field.

Introducing the magnetic vector potential A that satisfies the relations $\dot{A} = E$ and $A_z = B$ allows us to write the primitive Maxwell–Schrödinger equations as stationarity conditions for Hamilton's principle, $\delta \mathbf{S} = 0$, with action $\mathbf{S}$ given by

$$\mathbf{S} = \iint \left[\tfrac{1}{2}\dot{A}^2 - \tfrac{1}{2}A_z^2 + 2\kappa \dot{A}(a_+ a_-^* + a_+^* a_-) - (|a_+|^2 - |a_-|^2) + \mathrm{i}\kappa\left(a_+^* \dot{a}_+ - a_+ \dot{a}_+^* + a_-^* \dot{a}_- - a_- \dot{a}_-^*\right)\right] \mathrm{d}z\, \mathrm{d}t.$$

The third term in the integrand of $\mathbf{S}$ is the interaction term, which couples the electromagnetic field to the matter fields. Stationary variations with respect to A, a_+^* and a_-^* now give

$$\delta A: \quad \ddot{A} + 2\kappa \dot{P} - A_{zz} = 0,$$

$$\delta a_+^*: \quad \mathrm{i}\dot{a}_+ - \frac{1}{2\kappa} a_+ + E a_- = 0,$$

$$\delta a_-^*: \quad \mathrm{i}\dot{a}_- + \frac{1}{2\kappa} a_- + E a_+ = 0.$$

Passing to the Hamiltonian description via the usual Legendre transformation gives the conserved Hamiltonian

$$\mathbf{H} = \int \left(\tfrac{1}{2}E^2 + \tfrac{1}{2}B^2 + |a_+|^2 - |a_-|^2\right) \mathrm{d}z,$$

which is just the sum of the field energy and atomic excitation energy. This leads to a Hamiltonian formulation of the primitive Maxwell–Schrödinger equations using the canonical Poisson bracket for the fields,

$$\{\mathbf{G}, \mathbf{H}\} = \int \left[\left(\frac{\delta \mathbf{G}}{\delta A} \frac{\delta \mathbf{H}}{\delta D} - \frac{\delta \mathbf{G}}{\delta D} \frac{\delta \mathbf{H}}{\delta A} \right) - \frac{\mathrm{i}}{2\kappa} \left(\frac{\delta \mathbf{G}}{\delta a_+} \frac{\delta \mathbf{H}}{\delta a_+^*} - \frac{\delta \mathbf{G}}{\delta a_+^*} \frac{\delta \mathbf{H}}{\delta a_+} \right) - \frac{\mathrm{i}}{2\kappa} \left(\frac{\delta \mathbf{G}}{\delta a_-} \frac{\delta \mathbf{H}}{\delta a_-^*} \frac{-\delta \mathbf{G}}{\delta a_-^*} \frac{\delta \mathbf{H}}{\delta a_-} \right) \right] \mathrm{d}z.$$

In terms of the fields D and B, the first part of this Poisson bracket may also be written as

$$\int \left[\frac{\delta \mathbf{G}}{\delta D} \left(\partial_z \frac{\delta \mathbf{H}}{\delta B} \right) - \left(\partial_z \frac{\delta \mathbf{G}}{\delta B} \right) \frac{\delta \mathbf{H}}{\delta D} \right] \mathrm{d}z.$$

Hence,

$$\dot{A} = \{A, \mathbf{H}\} = \frac{\delta \mathbf{H}}{\delta D} = E,$$

$$\dot{D} = \{D, \mathbf{H}\} = \partial_z \frac{\delta \mathbf{H}}{\delta B} = B_z,$$

and we recover Maxwell's equations, (C.2). Likewise, we have

$$\dot{a}_+ = \{a_+, \mathbf{H}\} = -\frac{\mathrm{i}}{2\kappa} \frac{\delta \mathbf{H}}{\delta a_+^*} = \frac{1}{2\kappa} a_+ - E a_-,$$

$$\dot{a}_- = \{a_-, \mathbf{H}\} = -\frac{\mathrm{i}}{2\kappa} \frac{\delta \mathbf{H}}{\delta a_-^*} = -\frac{1}{2\kappa} a_- - E a_+,$$

for the atomic level amplitudes.

We now return to the action principle and write the atomic amplitudes in the "rotating wave" form,

$$a_+ = b_+ \mathrm{e}^{-\mathrm{i}(t-z)/2\kappa}, \quad a_- = b_- \mathrm{e}^{\mathrm{i}(t-z)/2\kappa}.$$

Also, we take the self-consistent part of the vector potential to be a modulated right-going wave, in the envelope form,

$$A = \mathrm{i}\kappa \mathscr{A}\, \mathrm{e}^{-\mathrm{i}(t-z)/\kappa} - \mathrm{i}\kappa \mathscr{A}^*\, \mathrm{e}^{\mathrm{i}(t-z)/\kappa},$$

with complex envelope function $\mathscr{A}$. In these expressions, the complex envelope functions b_+, b_- and $\mathscr{A}$ are assumed to depend only on time, t. Hence,

$$\tfrac{1}{2}\dot{A}^2 - \tfrac{1}{2}A_z^2 = -\mathrm{i}\kappa(\mathscr{A}\dot{\mathscr{A}}^* - \mathscr{A}^*\dot{\mathscr{A}}),$$

and

$$\mathrm{i}(a_+^* \dot{a}_+ - a_+ \dot{a}_+^*) = \mathrm{i}(b_+^* \dot{b}_+ - b_+ \dot{b}_+^*) - \frac{1}{\kappa}|b_+|^2,$$

$$\mathrm{i}(a_-^* \dot{a}_- - a_- \dot{a}_-^*) = \mathrm{i}(b_-^* \dot{b}_- - b_- \dot{b}_-^*) + \frac{1}{\kappa}|b_-|^2.$$

In the interaction term of the action we also add to the vector potential the perturbation piece

$$i\kappa'\epsilon\, e^{-i(t-z)/\kappa'} - i\kappa'\epsilon\, e^{i(z-z)/\kappa'},$$

where $1/\kappa - 1/\kappa' = \omega$, in order to represent the externally imposed probe laser field. Averaging over the fast phases, performing the z-integration, dividing by 4κ, and dropping terms of higher order in κ yields the new action

$$\begin{aligned}\mathscr{S} = \int \Big[& i(\mathscr{A}^*\dot{\mathscr{A}} - \mathscr{A}\dot{\mathscr{A}}^*) + i\big(b_+^*\dot{b}_+ - b_+\dot{b}_+^*\big) \\ & + i\big(b_-^*\dot{b}_- - b_-\dot{b}_-^*\big) + (\mathscr{A} + \epsilon\, e^{i\omega t})b_+^* b_- \\ & + (\mathscr{A}^* + \epsilon\, e^{-i\omega t})b_+ b_-^* \Big]\, dt.\end{aligned}$$

Varying the action $\mathscr{S}$ yields

$$\begin{aligned}\delta\mathscr{S} = \int \Big\{ & \delta\mathscr{A}^* \big(i\dot{\mathscr{A}} + b_+ b_-^*\big) \\ & + \delta\mathscr{A}\big(-i\dot{\mathscr{A}}^* + b_+^* b_-\big) \\ & + \delta b_+^* \big[i\dot{b}_+ + (\mathscr{A} + \epsilon\, e^{i\omega t})b_-\big] \\ & + \delta b_+ \big[-i\dot{b}_+^* + (\mathscr{A}^* + \epsilon\, e^{-i\omega t})b_-^*\big] \\ & + \delta b_-^* \big[i\dot{b}_- + (\mathscr{A}^* + \epsilon\, e^{-i\omega t})b_+\big] \\ & + \delta b_- \big[-i\dot{b}_-^* + (\mathscr{A} + \epsilon\, e^{i\omega t})b_-^*\big] \Big\}\, dt.\end{aligned}$$

Thus, stationarity of the averaged action $\mathscr{S}$ implies the Maxwell–Schrödinger envelope equations (2.1), provided we identify $\mathscr{A} = \mathscr{E}$, which follows to first order in κ from the relation $\dot{A} = E$ and the envelope form of the solution for the vector potential.

Via a Legendre transformation, the action $\mathscr{S}$ implies precisely the Hamiltonian formulation for eqs. (2.1) given in the text, with time-dependent Hamiltonian function given by the electromagnetic interaction energy,

$$\begin{aligned}\mathscr{H} = & -\tfrac{1}{2}(\mathscr{E} + \epsilon\, e^{i\omega t})b_+^* b_- \\ & -\tfrac{1}{2}(\mathscr{E}^* + \epsilon\, e^{-i\omega t})b_+ b_-^*.\end{aligned}$$

References

[1] H. Haken, Analogy between higher instabilities in fluids and lasers, Phys. Lett. A 53 (1975) 77–80.

[2] L. Allen and J.H. Eberly, Optical Resonance and Two-Level Atoms (Dover, New York, 1987).

[3] F.T. Arecchi and E.O. Schulz-Dubois, Laser Handbook, Vols. 1, 2 (North-Holland, Amsterdam, 1972).

[4] H. Haken, Light, Vol. 2, Laser Light Dynamics (North-Holland, Amsterdam, 1985).

[5] K. Shimoda, Introduction to Laser Physics, 2nd Ed., Springer Series on Optical Sciences, Vol. 44 (Springer, Berlin, 1986).

[6] J.V. Moloney and A.C. Newell, Nonlinear optics, Physica D 44 (1990) 1–37.

[7] F.T. Arecchi, Order and chaos in quantum optics, Acta Phys. Austr. 56 (1984) 57–74.

[8] P.I. Belobrov, G.M. Zaslavskii and G. Kh. Tartakovskii, Stochastic breaking of bound states in a system of atoms interacting with a radiation field, Sov. Phys. JETP 44 (1976) 945–951.

[9] P.I. Belobrov, G.P. Berman, G.M. Zaslavskii and A.P. Slivinskii, Stochastic mechanism of excitation of molecules that interact with their own radiation field, Sov. Phys. JETP 49 (1979) 993–997.

[10] P.W. Milonni, J.R. Ackerhalt and H.W. Galbraith, Chaos in the semiclassical N-atom Jaynes–Cummings model: Failure of the rotating-wave approximation, Phys. Rev. Lett. 50 (1983) 966–969.

[11] K.N. Alekseev and G.P. Berman, Dynamic chaos in the interaction between external monochromatic radiation and a two-level medium, with allowance for cooperative effects, Sov. Phys. JETP 65 (1987) 1115–1120.

[12] E.T. Jaynes and F.N. Cummings, Comparison of quantum and semiclassical radiation theories with applications to the beam maser, Proc. IEEE 51 (1963) 89–109.

[13] M. Tavis and F.W. Cummings, Exact solution for an N-molecule–radiation-field Hamiltonian, Phys. Rev. 170 (1968) 379–384.

[14] M. Born and E.B. Wolf, Principles of Optics, 6th (corrected) Ed. (Pergamon, Oxford, 1986).

[15] R.P. Feynman, F.L. Vernon Jr. and R.W. Hellwarth, Geometrical representation of the Schrödinger equation for solving maser problems, J. Appl. Phys. 28 (1957) 49–52.

[16] R. Devaney, Homoclinic orbits in Hamiltonian systems, J. Diff. Eqns. 21 (1976) 431–438.

[17] E.A. Coddington and N. Levinson, Theory of Ordinary Differential Equations (McGraw-Hill, New York, 1955).

[18] J. Hale, Ordinary Differential Equations (Robert E. Krieger, Malabar, FL, 1980).

[19] H. Poincaré, Les Méthodes Nouvelles de la Mécanique Céleste, 3 vols. (Gauthier–Villars, Paris, 1899).

[20] V.K. Melnikov, On the stability of the center for time periodic perturbations, Trans. Moscow Math. 12 (1963) 1–57.

[21] V.I. Arnold, Instability of dynamical systems with many degrees of freedom, Sov. Math. Dokl. 5 (1964) 581–585.

[22] P.J. Holmes, A nonlinear oscillator with a strange attractor, Philos. Trans. R. Soc. A 292 (1979) 419–448.

[23] P.J. Holmes and J.E. Marsden, Horseshoes in perturbation of Hamiltonian systems with two degrees of freedom, Commun. Math. Phys. 82 (1982) 523–544.

[24] P.J. Holmes and J.E. Marsden, Melnikov's method and Arnold diffusion for perturbations of integrable Hamiltonian systems, J. Math. Phys. 23 (1982) 669–675.

[25] L.M. Lerman and Ia. L. Umanski, On existence of separatrix loops in four dimensional systems similar to integrable Hamiltonian systems, Prikl. Mat. Mekh. 47 (1984) 335–340.

[26] C. Robinson, Horseshoes for autonomous Hamiltonian systems using the Melnikov integral, Ergod. Theory Dynam. Sys. 8* (1988) 395–409.

[27] S. Wiggins, Global Bifurcations and Chaos: Analytical Methods (Springer, New York, 1988).

[28] J. Moser, On the generalization of a theorem of A. Liapounoff, Commun. Pure Appl. Math. 11 (1957) 257–271.

[29] R. Bonifacio and L.A. Lugiato, Cooperative radiation processes in two-level systems: superfluorescence, Phys. Rev. A 11 (1975) 1507–1521.

[30] I.P. Gabitov, V.E. Zakharov and A.V. Mikhailov, Nonlinear theory of superfluorescence, Sov. Phys. JETP 59 (1984) 703–709.

[31] M.B. Spencer and W.E. Lamb Jr., Laser with a transmitting window, Phys. Rev. A 5 (1972) 884–892.

[32] G. Khitrova, J.F. Valley and H.M. Gibbs, Gain–feedback approach to optical instabilities in sodium vapor, Phys. Rev. Lett. 60 (1988) 1126–1129.

[33] V. Brundsen and P.J. Holmes, Power spectra of strange attractors near homoclinic orbits, Phys. Rev. Lett. 58 (1987) 1699–1702.

[34] V. Brundsen, J. Cortell and P.J. Holmes, Power spectra of chaotic vibrations of a buckled beam, J. Sound Vib. 130 (1989) 1–25.

[35] D.D. Holm, Gregor Kovačič and Bala Sundaram, Chaotic laser–matter interaction, Phys. Lett. A 154 (1991) 346–352.

[36] J. Guckenheimer and P.J. Holmes, Nonlinear Oscillations, Dynamical Systems, and Bifurcations of Vector Fields (Springer, New York, Heidelberg, Berlin, 1983).

[37] R. Abraham and J.E. Marsden, Foundations of Mechanics, 2nd Ed. (Addison–Wesley, Redwood City, CA, 1985).

[38] V.I. Arnold, Mathematical Methods of Classical Mechanics, 2nd Ed. (Springer, New York, Berlin, Heidelberg, 1989).

[39] P.J. Olver, Applications of Lie Groups to Differential Equations, 2nd Ed. (Springer, New York, Berlin, Heidelberg, 1986).

[40] J. Opt. Soc. B 5 (1988), special issue on Nonlinear Dynamics of Lasers.